Noname manuscript No.
(will be inserted by the editor)

Neutrino emission from binary neutron star mergers: characterizing light curves and mean energies

Marco Cusinato[1], Federico Maria Guercilena[2,3], Albino Perego[3,2], Domenico Logoteta[4,5], David Radice[6,7,8], Sebastiano Bernuzzi[9], Stefano Ansoldi[10]

[1]Dipartimento di Fisica, Università di Trieste, Via A. Valerio 2, 34127 Trieste, Italy
[2]INFN-TIFPA, Trento Institute for Fundamental Physics and Applications, via Sommarive 14, I-38123 Trento, Italy
[3]Dipartimento di Fisica, Università di Trento, Via Sommarive 14, 38123 Trento, Italy
[4]Dipartimento di Fisica, Università di Pisa, Largo B. Pontecorvo, 3 I-56127 Pisa, Italy
[5]INFN, Sezione di Pisa, Largo B. Pontecorvo, 3 I-56127 Pisa, Italy
[6]Institute for Gravitation and the Cosmos, The Pennsylvania State University, University Park, PA 16802, USA
[7]Department of Physics, The Pennsylvania State University, University Park, PA 16802, USA
[8]Department of Astronomy & Astrophysics, The Pennsyvlania State University, University Park, PA 16802, USA
[9]Theoretisch-Physikalisches Institut, Friedrich-Schiller Universität Jena, 07743, Jena, Germany
[10]Dipartimento di Scienze Matematiche, Informatiche e Fisiche, Univerità degli Studi di Udine, via delle Scienze 206, I-33100 Udine, Italy

November 29, 2021

Abstract Neutrinos are copiously emitted by neutron star mergers, due to the high temperatures reached by dense matter during the merger and its aftermath. Neutrinos influence the merger dynamics and shape the properties of the ejecta, including the resulting r-process nucleosynthesis and kilonova emission. In this work, we analyze neutrino emission from a large sample of merger radiation hydrodynamics simulations in Numerical Relativity, covering a broad range of initial masses, nuclear equation of state and viscosity treatments. We extract neutrino luminosities and mean energies, and compute quantities of interest such as the peak values, peak broadnesses, time averages and decrease time scales. We provide a systematic description of such quantities, including their dependence on the initial parameters of the system. We find that for equal-mass systems the total neutrino luminosity (several 10^{53}erg s^{-1}) decreases for increasing reduced tidal deformability, as a consequence of the less violent merger dynamics. Similarly, tidal disruption in asymmetric mergers leads to systematically smaller luminosities. Peak luminosities can be twice as large as the average ones. Electron antineutrino luminosities dominate (initially by a factor of 2-3) over electron neutrino ones, while electron neutrinos and heavy flavour neutrinos have similar luminosities. Mean energies are nearly constant in time and independent on the binary parameters. Their values reflect the different decoupling temperature inside the merger remnant. Despite present uncertainties in neutrino modelling, our results provide a broad and physically grounded characterization of neutrino emission, and they can serve as a reference point to develop more sophisticated neutrino transport schemes.

Keywords Relativistic Transport and Hydrodynamics · Compact Stars · Hadronic and Electroweak Interactions of Hadrons

PACS 04.25.D · 97.60.Jd · 97.80.-d · 14.60.Lm

1 Introduction

The study of binary neutron star (BNS) mergers represents one of the main topics in modern astrophysics. Due to the wide range of densities and temperatures required to study the dynamics of these events [1], their understanding requires to connect several branches of physics spanning from ordinary nuclear physics to hydrodynamics in extreme conditions under strong gravitational field. BNS mergers can be considered natural laboratories to investigate the behaviour of matter at extreme densities, which cannot be produced in Earth-based facilities (see e.g. [2, 3, 4] for recent reviews).

BNS mergers are one of the most interesting sources of gravitational waves (GWs) [5, 6], and a primary target for ground-based GW detector facilities such as LIGO [7], VIRGO[8] and KAGRA [9]. Furthermore, BNS mergers have long been considered one of the most likely progenitors of high-energy astronomical signals such as short gamma ray bursts (sGRBs) [10, 11, 12, 13]

and kilonovae [14, 15], see also [16, 17] for recent reviews. Kilonovae (sometimes also referred to as macronovae) are powered by the decay of radioactive heavy elements that are synthesized in the ejecta of BNS mergers [see e.g. 18, 19, and references therein]. This aspect links these systems to open issues regarding the evolution of the chemical composition of the Galaxy and of the Cosmos. BNS mergers have indeed emerged as sites (perhaps the main ones) of production of heavy elements in the Universe [20, 21, 22, 23].

All these hypotheses have recently received a direct confirmation by the first multimessenger detection of a BNS merger. In this event (hereafter GW170817) a GWs emission [24] was observed, followed by a sGRB (GRB170817A) and, finally, by a kilonova lasting from a few hours to several days after the merger [25, 26, 27, 28, 29, 23, 30, 31, 32, 33, 34, 35, 21, 36, 37, 38, 39, 40, 41, 42, 43, 44, 45]. This detection opened the era of multimessenger astronomy from compact binary mergers. A second detection of a GW signal from a BNS merger, GW190425 [46], was observed a couple of years later, but without the firm identification of associated electromagnetic counterparts.

BNS mergers produce copious amounts of neutrinos, starting from the latest moments of the inspiral until the merger remnant collapses or cools down. This emission actually is a key element in the dynamics of the system [10]. On one hand, neutrinos are thought to play a significant role in the jet-launching mechanism that powers sGRBs. Neutrino absorption and energy deposition in the funnel above the poles of the merger remnant could contribute to clean this region, reducing its baryon density and allowing the launch of a relativistic jet. It has also been suggested that neutrino/antineutrino pair annihilation could deposit an amount of energy compatible with the one necessary to explain sGRBs [see e.g. 10, 47, 48, 49, 50, 51, 52, 53]. Neutrino absorption is also likely one of the mechanisms for matter ejection from BNS mergers, in association to the production of neutrino-driven winds on time scales of $\sim 100\,\mathrm{ms}$ after the merger [e.g. 48, 50, 54, 53, 53]. Even more importantly, neutrino-matter interactions also affect the composition of the ejecta, in particular by driving the evolution of the relative abundance of neutrons and protons, starting from the decompression of beta-equilibrated, cold neutron star (NS) matter. The neutron richness in the ejecta directly impacts the outcome of the r-process nucleosynthesis and of the resulting kilonova signal [55, 56, 57]. It was shown that the neutrino transport used in the simulations impact on essential ejecta properties like the radial speed, the electron fraction and the entropy [58, 59, 60]. To reliably model these phenomena it is therefore of the utmost importance to characterize the properties of neutrino emission in BNS mergers.

BNS mergers are intrinsically multi-dimensional events. Moreover, their thermodynamic conditions are such that the neutrino optical depth decreases by several orders of magnitude from the optically thick central remnant to the optically thin accretion disc [61]. The quantitative modelling of neutrino production and diffusion in BNS mergers is, thus, a non-trivial task that has only been made possible by the advent of sophisticated numerical simulations in three spatial dimensions. The employed transport methods range from light bulb models in Newtonian spacetime, to moment schemes, and even to Monte Carlo schemes in full general relativity (GR) [e.g. 47, 62, 63, 64, 65, 66, 67, 68, 69, 70, 71, 72]. Despite being in its infancy, the field built upon the progress in our understanding of neutrino physics and transport in Core Collapse Supernova (CCSN) [73, 74, and references therein]. However, compared to the wealth of literature regarding neutrinos in CCSNe, only few studies in the past have examined neutrino luminosities and mean energies in BNS mergers [47, 62, 75, 76, 77, 58, 78, 79, 80]. From these seminal studies, a few robust features emerged. Due to the initial neutron richness, electron antineutrinos dominate over the other flavours. Moreover, heavy flavour neutrinos are more energetic, since they decouple deeper inside the remnant. Additionally, more compact BNSs produce more violent mergers, resulting in larger neutrino luminosities. Despite the general consensus about these features, quantitative differences have emerged, such that, both, the absolute and the relative importance of the different neutrino species, as well as their temporal evolution during the transition between the merger and the remnant cooling phase still remain largely unexplored. One of the main reasons behind these limitations is that neutrino luminosities are only studied for a few milliseconds, while neutrino cooling is relevant during the entire cooling phase, lasting up to tens of seconds.

In this work, we consider BNS simulations spanning a wide range in total mass, mass ratio, and dense matter equation of state (EOS). Moreover, we consider some of the longest BNS merger simulations in 3+1 numerical relativity (NR). We also consider the effects of the inclusion of physical viscosity of magnetic origin in our simulations. Based on this ample trove of data, we endeavour to find patterns, trends and commonalities in the temporal evolution of the neutrino luminosities and mean energies. We strive to identify in neutrino data universal relations, i.e., relations between parameters describing neutrino emission and quantities characterizing BNS models that are EOS independent. Similar relations have been found in the context of NS structure

and GW emission [81, 82, 83, 84, 85, 86, 87]. The broad scope of our data sample, which allows us to avoid as much as possible being biased towards a too specialised subset of BNS merger configurations, represents a major innovation of this work. All the simulations considered in this work are homogeneous with respect to the neutrino physics input and to the transport scheme. In particular, the minimal set of necessary neutrino reactions has been included (see the main text and Table 1 for details). Moreover, neutrino transport is taken in account using the combination of a leakage scheme and a so-called M0 scheme. These schemes attempt to strike a balance between computational cost and physical realism. In our setup, neutrinos are assumed to be massless and we neglect neutrino oscillations.

The paper is organized as follows: in Sec. 2 we summarize the numerical methods employed to perform the simulations, which we base our analysis on; Sec. 3 describes our simulation sample, the overall properties of neutrino emission, and the analysis strategy that we follow; Sec. 4 contains the main results of this work, in the form of a detailed analysis of the properties of neutrino emission in BNS mergers and their likely explanation in terms of the system dynamics. We discuss our results in the context of multimessenger astrophysics in Sec. 5. We finally summarize our findings and discuss their implications in Sec. 6. Several appendices provide additional details on our analysis, including information about each simulation in our sample.

2 Methods

2.1 Numerical setup

We base our analysis on results collected from a large sample of BNS mergers simulations in NR. All simulations share the same numerical setup and evolution scheme. In the following, we summarize them and we briefly introduce the codes used to produce our data. More details can be found in Ref. [88].

The BNS initial data are generated by the `LORENE` code (see Sec. 2.2 for details), and evolved with the infrastructure provided by the `Einstein Toolkit` [89, 90, 91]. The hyperbolic sector of Einstein's field equations is evolved with the Z4c formalism [92], implemented in the `CTGamma` solver [93, 94]. Moreover, general relativistic hydrodynamics is handled by the `WhiskyTHC` code [95, 96, 97, 98, 88]. The code solves Euler's equations for the balance of energy and momentum:

$$\nabla_\nu T^{\mu\nu} = Q u^\mu \,, \tag{1}$$

where $T^{\mu\nu}$ is the stress-energy tensor and Q is the net energy deposition rate due to the absorption and emission of neutrinos and antineutrinos (see Sec. 2.3.1). `WhiskyTHC` evolves neutron and proton number densities separately as:

$$\nabla_\mu \left(n_{\rm p,n} u^\mu\right) = R_{\rm p,n}, \tag{2}$$

where $n_{\rm p,n}$ are the proton and neutron number densities, respectively, u^μ is the fluid four-velocity and $R_{\rm p,n}$ is the net lepton number exchange rate due to the absorption and emission of electron flavour neutrinos and antineutrinos. Due to charge neutrality the electron fraction is directly related to the proton number density, i.e. $Y_{\rm e} \equiv n_{\rm e}/(n_p + n_n) = n_{\rm p}/(n_p + n_n)$. Neutrino emission and cooling are handled with a leakage scheme, while neutrino absorption and heating in optically thin conditions are treated with the so-called M0 scheme (see Sec. 2.3.1). Eqs. (1) and (2) are closed by a finite-temperature, composition dependent, nuclear EOS (see Sec. 2.3.2). The code also implements the general-relativistic large-eddy simulation (GRLES) method to account for turbulent viscosity of magnetic origin (see Sec. 2.3.3).

The computational domain of the simulations is a cube of side $\sim 3024\,$km centred on the binary's centre of mass. The code uses a box-in-box Berger-Oliger adaptive mesh refinement (AMR) scheme with refluxing [99, 100] provided by the `Carpet` module of the `Einstein Toolkit`, and composed of seven refinement levels. The finest refinement level covers both NSs during the inspiral and the remnant after the merger, and it has a resolution of $h \approx 246\,$m (for grid setup named here low resolution; LR), $h \approx 185\,$m (standard resolution; SR) or $h \approx 123\,$m (high-resolution; HR) [see also 101].

2.2 Relevant simulation parameters

Each BNS is characterized by the gravitational masses of the two NSs at infinity, $M_{A,B}$[1]. The total gravitational mass and mass ratio are defined as $M_{\rm tot} = M_A + M_B$ and $q = M_A/M_B$, respectively. A further characterization of the initial properties of each BNS system is provided by the dimensionless reduced tidal deformability $\tilde{\Lambda}$, since it also depends on the stars' EOS. It is a weighted average of the dimensionless tidal deformabilities Λ_i, $i \in A, B$, of the two NSs, defined as [102]:

$$\tilde{\Lambda} = \frac{16}{3} \frac{\left(M_A + 12 M_B\right) M_A^4 \Lambda_A}{M_{\rm tot}^5} + \left(A \leftrightarrow B\right). \tag{3}$$

In Eq. (3) the notation $(A \leftrightarrow B)$ indicates a second term identical to the first except that the indices A and

[1] Here and in the following the subscripts A and B refer to the most and least massive star of a BNS system, respectively.

B are exchanged. The dimensionless tidal deformabilities in turn are related to the quadrupolar Love number, k_2, describing the static quadrupolar deformation of a star in the gravitoelectric field of the companion [103], by:

$$\Lambda_i = \frac{2}{3} k_2 C_i^{-5} \,, \tag{4}$$

where $C_i = GM_i/c^2 R_i$ is the NS compactness.

The initial data for all the selected simulations are constructed by solving for irrotational stars of varying masses and different EOSs, using the spectral elliptic solver `LORENE` [104]. The binaries are set to quasi-circular orbits at an initial separation which, in most cases, is 45 km. This orbital separation corresponds to an inspiral phase of $2-3$ orbits before merger. Note that our results do not depend sensitively on the initial separation or the number of orbits before merger, since neutrino emission is linked to the dynamics of the system in the post-merger phase. The EOS used in solving for the initial data are the minimum temperature slice of the EOS table used for the evolution composition fixed assuming neutrinoless beta-equilibrium.

In the following, we use the term *model* to describe a BNS system with a given combination of initial masses and EOS. For each model, we can have multiple realizations of it, i.e. *simulations*, which differ from one another by having been run at different resolution, or by including or not a model of the magnetic viscosity of turbulent origin.

2.3 Input physics

2.3.1 Neutrino transport

Since the focus of the present work are the properties of neutrino emission, we provide here a brief, yet fairly detailed, description of the methods of neutrino transport implemented in the simulations that we use. These methods (a leakage scheme and the so-called M0 scheme) are described in detail in Refs. [64, 98] and references therein. They are both "grey" schemes, i.e. schemes in which the dependence of various quantities on the energy of the neutrinos is not explicitly taken into account: instead, energy-averaged quantities are considered. They account for three distinct neutrino species: electron neutrinos, $\nu_{\rm e}$; electron antineutrinos, $\bar{\nu}_{\rm e}$; and a collective species for heavy neutrinos, $\nu_{\rm x}$. The last one models muonic and tauonic neutrinos and antineutrinos as a single species of statistical weight 4.

Neutrino emission. The emission of neutrinos from the fluid and the subsequent loss of energy (i.e. cooling) is described by a neutrino leakage scheme (NLS). It is based on the method outlined in Ref. [105], where the local thermodynamical equilibrium chemical potential is used everywhere for all neutrino species while computing opacities as in Ref. [106]. Table 1 lists the reactions taken into account by this scheme to compute the neutrino production free rates, $R_\nu^{\rm free}$, $\nu \in \{\nu_{\rm e}, \bar{\nu}_{\rm e}, \nu_{\rm x}\}$, the free energy release, $Q_\nu^{\rm free}$, and the neutrino absorption, $\kappa_{\nu,{\rm a}}$, and scattering, $\kappa_{\nu,{\rm s}}$, opacities. These reactions include charged current absorption reactions on free nucleons, namely electron neutrino and antineutrino absorption on free neutrons and protons, respectively; and their inverse reactions. The direct ones are the main responsible for the absorption of $\nu_{\rm e}$ and $\bar{\nu}_{\rm e}$ both in optically thick and thin conditions, and they provide a relevant contribution to neutrino opacity. The inverse ones are the main processes responsible for the production of electron neutrinos and antineutrinos in hot and dense matter. Additionally, we consider the production of neutrino pairs of all flavours through electron-positron annihilation, nucleon-nucleon bremsstrahlung and plasmon decay. The first one is expected to be the most relevant source of $\nu_{\rm x}$'s in mildly and non-degenerate matter conditions, while the second one at very high density [107, 108]. We neglect their explicit contribution to the absorption opacity, since we expect it to be subdominant due to the pair nature of the inverse reactions, even if their thermalization effect is implicitly taken into account inside a NLS. Neutrino scattering off free nucleons is included as a major source of scattering opacity for neutrinos of all flavours and it is treated in the elastic approximation. In the case of $\nu_{\rm e}$'s and $\bar{\nu}_{\rm e}$'s, this opacity contribution is comparable to the one of absorption reactions, while in the case of $\nu_{\rm x}$ this is the dominant one [see e.g. 61]. Coherent scattering off nuclei is also included, even if the paucity of nuclei makes its impact negligible in the context of BNS mergers. It is important to recall that, at leading order, both the absorption and the scattering opacity off free nucleons depends quadratically on the energy of the incoming neutrinos. This quadratic dependence is taken into account when computing absorption opacities for the M0 scheme.

The scheme distinguishes number density weighted opacities, $\kappa^0_{\nu,{\rm a}}$ and $\kappa^0_{\nu,{\rm s}}$, that determine the rate at which neutrinos diffuse out of the material, from energy density weighted opacities, $\kappa^1_{\nu,{\rm a}}$ and $\kappa^1_{\nu,{\rm s}}$, that determine the rate at which energy is released due to the loss of neutrinos. The neutrino optical depth τ_ν is evolved in time following the scheme presented in [109], which allows the optical depth profile to adapt to the complex geometry of the system. In particular, the optical depth

evolves as:

$$\tau_\nu^{n+1} = \max((k_{\nu,\mathrm{s}} + k_{\nu,\mathrm{a}})\mathrm{d}l + \tau_\nu^n)\,, \tag{5}$$

where $\mathrm{d}l$ is a local displacement of one grid point and the maximum is taken over all spatial directions.

The optical depth is used to define the effective emission rates:

$$R_\nu^{\mathrm{eff}} = \frac{R_\nu^{\mathrm{free}}}{1 + t^0_{\mathrm{diff}}(t^0_{\mathrm{loss}})^{-1}}\,, \tag{6}$$

where t_{diff} is the effective diffusion time:

$$t^0_{\mathrm{diff}} = \mathcal{D}\frac{(\tau^0_\nu)^2}{\kappa^0_{\nu,\mathrm{a}} + \kappa^0_{\nu,\mathrm{s}}}\,, \tag{7}$$

and t_{loss} is the neutrino emission time scale:

$$t^0_{\mathrm{loss}} = \frac{R_\nu^{\mathrm{free}}}{n_\nu}\,. \tag{8}$$

In Eq. (7), $\mathcal{D}$ is a (dimensionless) tuning parameter set to 6, and n_ν in Eq. (8) is the neutrino number density computed assuming thermal and weak equilibrium. The effective energy emission rates Q_ν^{eff} are computed with the same procedure as R_ν^{eff}, but using the appropriate opacities and optical depths. This method of computing effective rates mimics the diffusion of radiation in regions of high optical depth and its free emission in optically thin regions.

Neutrino transport and absorption in optically thin conditions. Neutrino transport and absorption in optically thin conditions is accounted for by the moment scheme introduced in [98], called M0 scheme. Neutrinos are split into two components: a free-streaming one, n_ν^{fs}, and a trapped one, n_ν^{trap}, which is treated with the NLS previously described. The M0 scheme evolves the zeroth moment of the distribution function of free streaming neutrinos, and allows to compute their number densities and average energies on a polar grid. This scheme assumes that neutrinos propagate radially at the speed of light along four-vectors:

$$k^\alpha = u^\alpha + r^\alpha\,, \tag{9}$$

where r^α represents the spatial direction of propagation orthogonal to the fluid four-velocity u^α. This assumption implies that the neutrino number current J^α equals $n_\nu^{\mathrm{fs}}k^\alpha$. Under these assumptions it is possible to show that the free-streaming neutrino number density, n_ν^{fs}, satisfies:

$$\nabla_\alpha(n_\nu^{\mathrm{fs}}k^\alpha) = R_\nu^{\mathrm{eff}} - \kappa_{\nu,\mathrm{a}}n_\nu^{\mathrm{fs}}\,, \tag{10}$$

where $\kappa_{\nu,\mathrm{a}}$ is the absorption opacity. This finally results in an evolution equation for the neutrino number density, namely:

$$\partial_t(\sqrt{-g}n_\nu^{\mathrm{fs}}k^t) + \partial_r(\sqrt{-g}n_\nu^{\mathrm{fs}}k^r) = \sqrt{-q}(R_\nu^{\mathrm{eff}} - \kappa_\nu^{\mathrm{eff}}n_\nu^{\mathrm{fs}})\,, \tag{11}$$

where g is the four-metric determinant in spherical coordinates. This equation is solved on a series of independent radial rays using a first order, fully-implicit, finite volume method.

Free-streaming neutrino mean energies are estimated under the additional assumption of a stationary spacetime. Accordingly, $t^\alpha := (\partial_t)^\alpha$ is assumed to be a Killing vector so that $p_\nu^\alpha(\partial_t)_\alpha$, with p^α being the neutrino four-momentum, is conserved. Therefore the quantity $\varepsilon_\nu = -p^\alpha t_\alpha$ represents the energy of neutrinos as seen by the "coordinate observer" (a non-physical observer with four-velocity t^α), and can be rewritten as $\varepsilon_\nu = E_\nu\chi$, with $\chi = -k_\alpha t^\alpha$. Within this approximation, the evolution equation for the average neutrino energy is written as:

$$n_\nu^{\mathrm{fs}}k^t\partial_t\varepsilon_\nu + n_\nu^{\mathrm{fs}}\partial_r\varepsilon_\nu = (\chi Q_\nu^{\mathrm{eff}} - \varepsilon_\nu R_\nu^{\mathrm{eff}})\,, \tag{12}$$

where Q_ν^{eff} and R_ν^{eff} are the effective neutrino energy and the effective neutrino emission rates taken from the NLS. This equation is solved using a fully-implicit upwind 1st order finite-difference method.

The coupling with the hydrodynamics is handled by interpolating quantities from/to the standard Cartesian AMR grid at every timestep. In the setup of our sample of simulations, the M0 grid consists of 2048 rays uniformly spaced in latitude and longitude with a radial resolution $\Delta r \approx 244\,\mathrm{m}$. The neutrino number and energy rates computed by the combined leakage and M0 schemes appear as sources in the Euler equations for the NS matter, see Sec. 2.1. The coupling in this case is handled, at every timestep, by first advancing the hydrodynamic quantities in time disregarding neutrino contributions; neutrino sources are then added to the Euler equations with a semi-implicit first-order method, in an operator split approach.

2.3.2 Equations of state

In our simulation sample, we consider six finite temperature, composition dependent EOSs, namely: LS220 [112], SLy4 [113, 114], DD2 [115, 116], SFHo [117], BHB$\Lambda\phi$ [118], and BLh [119]. They are widely used in the literature on BNS mergers and are broadly consistent with current constraints, including astrophysical constraints derived from GW observations [24, 120, 121, 46, 122]. The above EOSs satisfy properties of

Name	Reaction	Reference
Electron neutrino capture on free neutron	$\nu_e + n \leftrightarrow p + e^-$	[110]
Electron antineutrino capture on free protons	$\bar{\nu}_e + p \leftrightarrow n + e^+$	[110]
Electron-positron annihilation	$e^+ + e^- \rightarrow \nu + \overline{\nu}$	[105]
Plasmon decay	$\gamma + \gamma \rightarrow \nu + \overline{\nu}$	[105]
Nucleon-nucleon Bremsstrahlung	$N + N \rightarrow N + N + \nu + \overline{\nu}$	[108]
Scattering off nucleons	$\nu + N \rightarrow \nu + N$	[105]
Scattering off nuclei	$\nu + A \rightarrow \nu + A$	[111]

Table 1 Weak reactions accounted for in the neutrino transport schemes. The following notation is used: $N \in \{n, p\}$ denotes a free nucleon, A a nucleus, $\nu \in \{\nu_e, \bar{\nu}_e, \nu_x\}$ a neutrino. The "Reference" column accounts for the corresponding rate implementation.

symmetric nuclear matter at saturation density. They also provide values for the symmetry energy and its slope in agreement with recent experimental estimates [123, 124], with the possible exception of PREX II results [125] that reported a quite large value of the slope of the symmetry energy at saturation density. The matter modelled by these EOSs is composed of neutron, protons, electrons, positrons and photons. One of them, namely BHB$\Lambda\phi$, also includes the additional degree of freedom represented by Λ-hyperons.

The LS220 and SLy4 EOSs are based on a non-relativistic liquid drop model with a Skyrme-like interaction. This model includes surfaces effects and considers in the low density region an ideal classical gas formed by α particles and heavy nuclei. The latter are treated using the single nucleus approximation (SNA). The SLy4 EOS employed in this work is constructed on the original Skyrme parametrisation proposed in Ref. [113] for cold nuclear matter. It is extended to finite temperature [114], employing an improved version of the LS220 framework that includes non-local isospin asymmetric terms, a better treatment of nuclear surface properties, and a more consistent treatment of heavy nuclei sizes.

The DD2, SFHo, and BHB$\Lambda\phi$ EOSs are based on relativistic mean field (RMF) models. Besides single nucleons, their composition includes light nuclei (such as deuterium, tritium, helium) as well as heavy nuclei in nuclear statistical equilibrium (NSE). The Lagrangian that models the mean-field nuclear interaction is parametrised differently for the three EOSs. While DD2 and BHB$\Lambda\phi$ use density dependent coupling constants, the SFHo parametrisation employs constant couplings adjusted to reproduce NS radius measurements from low-mass X-ray binaries. In all three cases, the resulting RMF equations are solved in Hartree's approximation.

The BLh EOS is a microscopical, finite temperature EOS obtained as an extension to the zero-temperature BL EOS [126]. At densities larger than 0.05 fm^{-3}, the latter was derived in the framework of the non-relativistic many-body Brueckner-Hartree-Fock (BHF) approach. The nucleon-nucleon interactions are described through a potential derived in the context of chiral effective theory [127]. They include two-body interactions [128] calculated up to next-to-next-to-next-to-leading order (N3LO), and an effective treatment of three-body interaction up to next-to-next-to-leading order (N2LO) [129]. Both interactions include contributions from Δ-excitation in the intermediate states of the nucleon-nucleon and three-nucleon interactions. Finite temperature and arbitrary nuclear composition effects are calculated using the finite temperature extension of the Brueckner–Bethe–Goldstone quantum many-body theory in the BHF approximation. At low densities the BLh EOS is smoothly connected to the SFHo EOS.

The EOSs employed in this work have been chosen in order to cover a broad range of stiffness. The stiffest EOS is the DD2 EOS, while the softest is the SLy4 EOS. These two EOSs support cold, non-rotating NSs maximum masses of $2.42\,M_\odot$ and $2.06\,M_\odot$, respectively. Operating on a broad stiffness range is important on one hand to avoid as much as possible any bias in our analysis, and on the other to allow us to look for universal relations in our data, i.e. to look for trends that do not depend on the choice of a particular EOS.

2.3.3 Viscosity

Slightly more than one third of the models analysed in this work employs the GRLES method of Ref. [130] to investigate the impact of turbulent viscosity on the merger dynamics [see also 131, for an alternative version of this formalism].

In essence, the GRLES method consists in taking into account that, due to finite resolution, any simulation deals only with a coarse-grained version of the hydrodynamics equations. Formally, this means introducing a linear filtering operator on the hydrodynamics variables that removes features at small scales (in our case this is simply the the cell-averaging of the finite-volume discretization of the equations).

In turn, this implies that applying the filtering to the hydrodynamics equations requires the introduction of closure terms. In the resulting equations, the turbulent viscosity, $\nu_{\rm T}$, is expressed in terms of the sound speed, $c_{\rm s}$, and a free parameter, $\ell_{\rm mix}$, that sets the characteristic length at which the turbulence operates, as $\nu_{\rm T} = \ell_{\rm mix} c_{\rm s}$. In the simulations that we consider, $\ell_{\rm mix}$ is estimated as a function of the rest mass density by fitting the results of very high resolution magnetohydrodynamics (MHD) BNS merger simulations [132, 133].

3 Overview of simulations and analysis methods

3.1 Simulations sample

For our analysis, we consider a subset of the simulations presented in Ref. [1], whose setup is generic and not targeted to model a specific BNS configuration. In addition, we consider a subset of the simulations targeted to GW170817 and extensively discussed in Refs. [101, 134, 135], and data extracted from more recent simulations targeted to GW190425 [136]. Finally, we include also eight simulations which have not been published in earlier works but are presented for the first time in this article. In summary, we work on a sample of 66 simulations of 51 models of BNS mergers. The range of total gravitational mass $M_{\rm tot}$ spanned by these models is $[2.600, 3.438]\, M_\odot$ and the range of mass ratio q is $[1.0, 1.82]$, corresponding to a wide range in both these relevant variables.

The reduced dimensionless tidal deformability of our set of models spans the wide range $\tilde{\Lambda} \in [90, 1108]$. By comparison, data from the only two detected GW signals compatible with BNS mergers, namely GW170817 and GW190425, suggest that for those systems $\tilde{\Lambda} < 700$ at the 90% confidence level [137]. However, we remind the reader that $\tilde{\Lambda}$ depends on the masses and mass ratio of the stars, so future events could also have larger $\tilde{\Lambda}$.

Regarding resolution, the sample consists of 15 LR simulations, 49 SR simulations, and 2 HR simulations. Where possible, we have decided to work with SR simulations because these tend to offer a better balance between accuracy and time extent of the post-merger data. Finally, 25 simulations out of the 66 employ the GRLES method described in Sec. 2.3.3 to account for viscous effects.

For each simulation, in addition to the detailed 3D profiles of all thermodynamics and spacetime quantities, we consider the neutrino energy luminosities and mean energies as extracted at the edge of the M0 computational domain and integrated over the outermost coordinate sphere. The luminosities and the mean energies are given in retarded time with respect to the time of merger (computed as the instant where the amplitude of the strain of the GW is maximum). The main properties of our sample of BNS simulations are summarized in Tables 2 and 3 in Appendix C.

3.2 Neutrino emission: a qualitative overview

We present first an overview of the observed properties of neutrino emission that are common to large subsets of models and simulations in our sample. According to the remnant fate, we distinguish our simulations into four categories: PC, VSL, DC and LL. We define PC simulations as the ones for which, at the time of merger, the minimum of the lapse function over the computational domain decreases monotonically, while the maximum of the rest mass density increases monotonically. These conditions provide a proxy for detecting the collapse of the central object to a black hole (BH), i.e. for all these simulations the remnant is too heavy to sustain the formation of an massive neutron star (MNS). BH formation usually happens in these cases within $\sim 2\,$ms after the merger. In VSL simulations, the merger remnant does not collapse promptly, but within 5 ms from the merger. DC simulations are those for which the collapse happens between 5 ms and the end of the simulation. Finally, in LL simulations no BH are observed until the simulation end. These definitions are indeed motivated by the mechanics of neutrino emission in BNS mergers. Since for the most part neutrinos are emitted by the central object and by the innermost part of the accretion disc, rather than by the outer part of the disc or by the ejecta, every simulation within one of these groups has similar properties and behaviour regarding neutrino luminosities and mean energies.

With reference to Fig. 1, we observe that in all cases the neutrino luminosity starts to increase just before the merger. During the inspiral, tidal interaction heats up the two NSs, however this effect is expected to be small, $T \lesssim 1\,$MeV [see e.g. 138], and not accompanied by an intense neutrino emission. However, a non-negligible luminosity is observed in our simulations also during the inspiral. This is due to a spurious numeric increase in temperature ($T \lesssim 10\,$MeV) at the NS surfaces resulting from the fast NS motion inside a much more dilute atmosphere. A more significant increase is observed around merger, due to the direct contact between the NS surfaces. This process continues during the merger and its immediate aftermath, causing the neutrino luminosity to peak at this time to typical values around $10^{53}\,{\rm erg\ s^{-1}} = 100\,$Bethe. This is primarily due to the rapid increase in matter temperature (up to

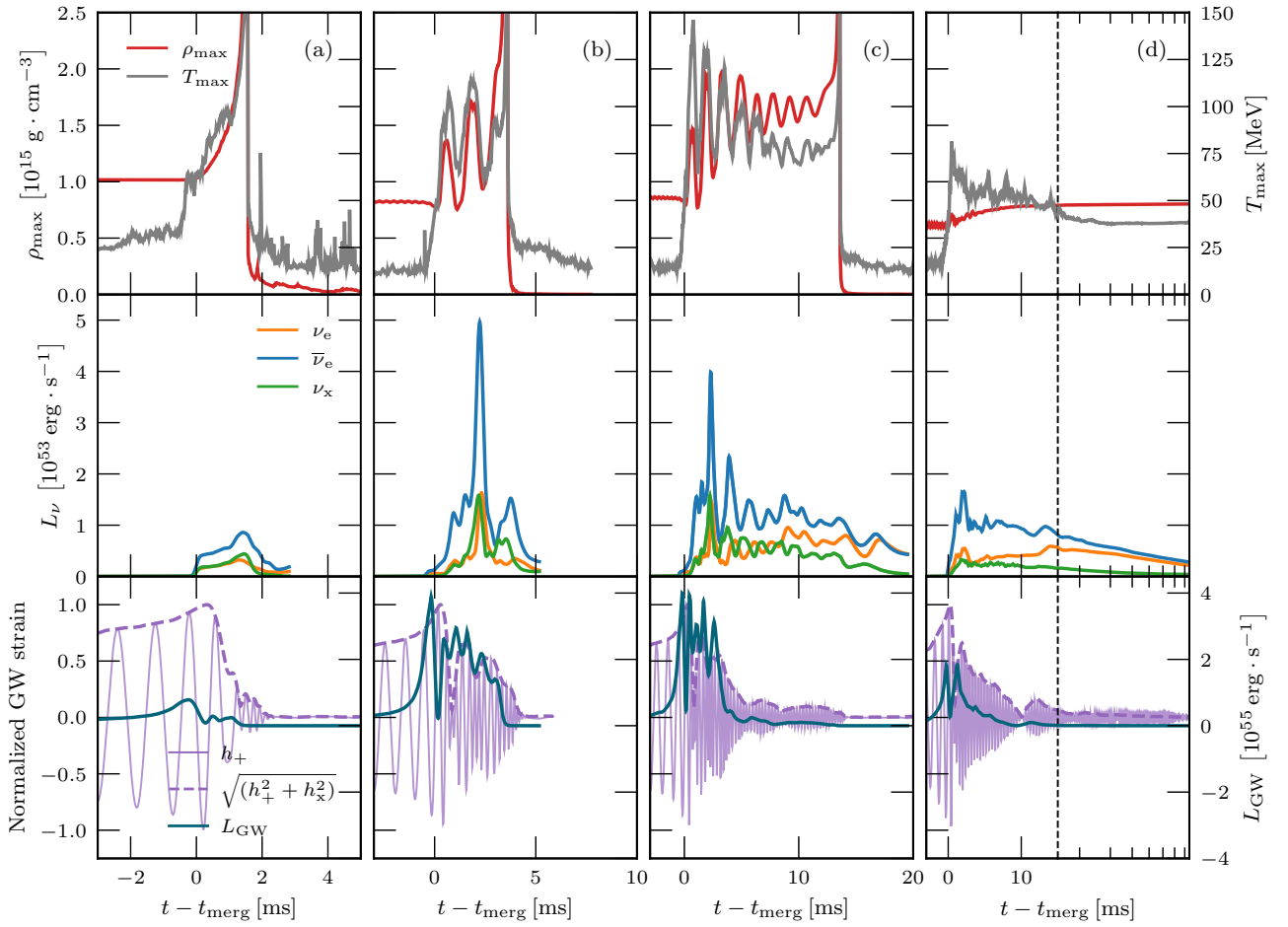

Fig. 1 Evolution of the maximum density and temperature (top panels), normalized GW strain and GW luminosity (middle panels), and neutrino luminosity for the three neutrino species (bottom panels) for four models representative of the considered simulation categories. (a): PC simulation with LS220 EOS, NS masses of $1.772M_\odot$ and $1.065M_\odot$, and no viscosity; (b): VSL simulation of an equal mass binary ($1.364M_\odot$) with SFHo EOS and no viscosity; (c): DC simulation of an equal mass binary ($1.364M_\odot$) with SLy4 EOS and no viscosity; (d): LL simulation with DD2 EOS, NS masses of $1.509M_\odot$ and $1.235M_\odot$, with viscosity.

several tens of MeV) due to the NS collision and core fusion, two processes in which kinetic bulk energy is efficiently converted into thermal energy available to be radiated in neutrinos.

PC simulations present a single, relatively low peak generally between the merger and one millisecond after it. This is due to the main source of neutrinos, the merger remnant, being cut off by its collapse. In VSL simulations this peak is also present, but typically a few times higher than for PC ones. By contrast, simulations that last more than 10 ms after the merger (DC and LL ones) have, typically, between 3 to 4 luminosity peaks in the first 10-15 ms after the merger for each neutrino flavour. We observe that in our sample the first peak is the highest one regardless of the EOS and mass ratio. These luminosity peaks are likely related to the oscillations of the MNS in the early post merger. In this phase, the contractions and expansions of the merger remnant as it evolves towards a more stable configuration drive shock waves outwards through the remnant itself and the surrounding matter, raising its temperature via shock heating and therefore enhancing neutrino emission. Additionally, matter compressed at the NS collision interface and between the two merging cores is heated up and expelled from the centre of the remnants, expanding and decreasing its density inside the forming accretion disc. It is however non-trivial to link neutrino luminosity peaks to, e.g., features in the density evolution of the MNS or in the GW signal, as Fig. 1 illustrates. This is due to the fact that neutrinos can escape the system only when produced or transported outside the neutrinosphere, which is located ~ 20 km from the remnant and is itself evolving

and growing in radius [61], making it very difficult to look for time coincidences.

Most VSL remnants approach a BH-torus configuration shortly after merger. We observe that after this point the neutrino luminosity decreases very rapidly, even if it does not drop to zero, as the inner, hot parts of the remaining disc are still neutrino sources. A similar behaviour can be seen in the DC case, but the drop in luminosity is not as steep as in VSL simulations and the post collapse luminosity is $\lesssim 50\%$ of the one before merger. This is due to the fact that the accretion disc mass is usually larger if the system is less massive (i.e. less prone to a fast collapse) or asymmetric (i.e. more prone to a tidal deformation of the secondary). Indeed, since the disc formation process lasts for several milliseconds after merger [88, 135], a faster collapse of the central MNS prevents the formation of a massive disc that can sustain a significant luminosity also after the MNS collapse. We recall, in this respect, that the collapse of the MNS drags inside the apparent horizon roughly half of the disc mass, corresponding to the innermost, hotter portion of the disc.

In the LL simulations, instead, due to the longer survival of the merger remnant, after the first oscillatory phase lasting between 10 and 15 ms, the neutrino luminosity decreases exponentially in time at a much smaller and steady rate, remaining comparable to the luminosity observed in the first milliseconds after merger on time scales even of hundreds of milliseconds, i.e. comparable to the MNS lifetime. In a MNS+disc configuration, both the central object and the disc significantly contribute to the neutrino emission. The cooling of the central object and the release of gravitational energy inside the accretion disc are both active mechanisms in sustaining the neutrino emission over the longer cooling and accretion time scales. In particular, the optical depth for the most relevant neutrino energies inside the disc is of the order of a few, while it is two to three orders of magnitude larger inside the central MNS. As a consequence, the cooling time scale of the disc is a few ms and its luminosity is sustained until accretion takes place, while the cooling time scale of the MNS is of several seconds and the corresponding luminosity lasts until the central object is hot enough [see e.g. 139]. In Ref. [140], it was estimated that a LL remnant should liberate $\sim 0.08 M_\odot c^2$ in its cooling phase. This corresponds to $\sim 1.4 \times 10^{53}$erg. This is compatible with a total neutrino luminosity of the order of 10^{53}-10^{52}erg s^{-1}, lasting for a few seconds.

Regarding the relative abundance of neutrino species, during and after the merger positron captures on free neutrons are favored since matter is initially extremely neutron rich ($Y_e \sim 0.1$) and hot ($T \sim 10 - 50$ MeV). Therefore the electron antineutrino luminosity is dominant in every model. For electron neutrinos the most relevant production reaction is the capture of electrons on free protons. Due to the relative paucity of protons, ν_e are emitted in a subdominant fashion with respect to $\bar{\nu}_e$. Moreover ν_e are also more easily absorbed in typically thin conditions in their way out from the remnant. Around the time of merger heavy flavour neutrinos are emitted with a luminosity comparable to that of electron neutrinos. However, heavy neutrinos are produced mostly by electron-positron annihilation and plasmon decay (see Table 1), reactions that have an extreme dependence on temperature (the relative production rates scale roughly as $Q_{\nu_x} \propto T^9$ [64]). On the other hand electron (anti-)neutrinos are mostly produced via electron/positron captures on nucleons, reactions with a milder dependence on the temperature. Therefore, as the system stabilizes and cools, the heavy neutrino production is reduced with respect to the other neutrino flavours. In the case of LL simulations, we also note that with time the difference in luminosity between ν_e and $\bar{\nu}_e$ tends to decrease, such that for all long lasting simulations we observe that $L_{\bar{\nu}_e} \sim L_{\nu_e}$. This is due to the matter being leptonized, reducing the dominance of the $\bar{\nu}_e$'s emission mechanisms.

The neutrino mean energies present a different pattern with respect to the neutrino luminosities. In the first few milliseconds after merger, we observe that they oscillate wildly and rapidly. However, this might be an artefact due to the approximate character of the neutrino transport schemes we rely on. We therefore do not attempt to characterize this phase any further. After this oscillatory phase the neutrino mean energies show a much more stable behaviour, in fact they are nearly constant until the end of simulation or the collapse to BH of the merger remnant. Clearly this second phase is only present in DC and LL simulations. This behaviour is related to the thermodynamic conditions of matter around the surfaces of neutrino decoupling. Neutrinos leave the system if emitted outside the neutrinosphere, and their energy distribution is strongly influenced by the temperature of the emitting medium at the density where thermal and weak decoupling between neutrinos and matter occurs. In the aftermath of BNS mergers, the neutrinospheres for each flavour and neutrino energy are mostly determined by the density profile inside the disc [61], and the latter changes very slowly, only over the accretion time scale. This in turn implies that the neutrinos are emitted by matter whose thermodynamic conditions do not significantly vary within the analysed time.

3.3 Analysis strategy

Based on the general features summarized in Sec. 3.2, we focus our analysis on neutrino luminosities L_ν and mean energies E_ν for all three flavours, i.e. for $\nu \in \{\nu_e, \bar{\nu}_e, \nu_x\}$.

For all simulations we consider the peak luminosity $L_{\mathrm{peak},\nu}$, which is simply the highest peak that the neutrino luminosity reaches over time for a given simulation. We also examine the full width at half maximum (FWHM) Γ of the peak by fitting the neutrino luminosity in a window of width 1 ms centred on the peak luminosity time t_{peak}. As a fitting function, we employ a Gaussian function:

$$L = L_{\mathrm{peak}} \exp\left(-\frac{(t - t_{\mathrm{peak}})^2}{2\sigma^2}\right), \tag{13}$$

where the amplitude and peak centre position are fixed as the peak luminosity and time, respectively, while the peak width σ is the fitting parameter. Finally the FWHM is related to σ as:

$$\Gamma = 2\sqrt{2\ln 2}\sigma\,. \tag{14}$$

For DC and LL simulations, we also analyze the values of the time-averaged luminosity $\langle L_\nu \rangle$ and the time-averaged neutrino mean energy $\langle E_\nu \rangle$. For the luminosity, the time average is computed using a window starting at the time of merger and extending either to 10 ms after merger or until BH formation. This window has been chosen to be long enough so that computing the average is meaningful, but not so long that in LL simulations the final value is influenced by the late time decrease. To these time-averages we associate their standard deviations, computed as:

$$\sigma_{L_\nu} = \sqrt{\langle L_\nu^2 \rangle - \langle L_\nu \rangle^2}\,, \tag{15}$$

where $\langle L_\nu^2 \rangle$ is the average of the squared luminosity. The standard deviation of the luminosity provides a way to characterize the deviations of the data from the mean value.

In a similar fashion we also compute time-averaged neutrino mean energies and their standard deviations. However, we select in this case a different time window, extending from the point at which the neutrino mean energies begin to stabilize (typically 2-5 ms after the merger), to either the end of the simulation or BH formation. In this case too the window has been chosen to be long enough to get a meaningful average energy. Differently from the case of the time-averaged luminosity however, the final computed value is not sensitive to the end point of the window, because as noted above mean energies are essentially constant until collapse or the end of the simulation.

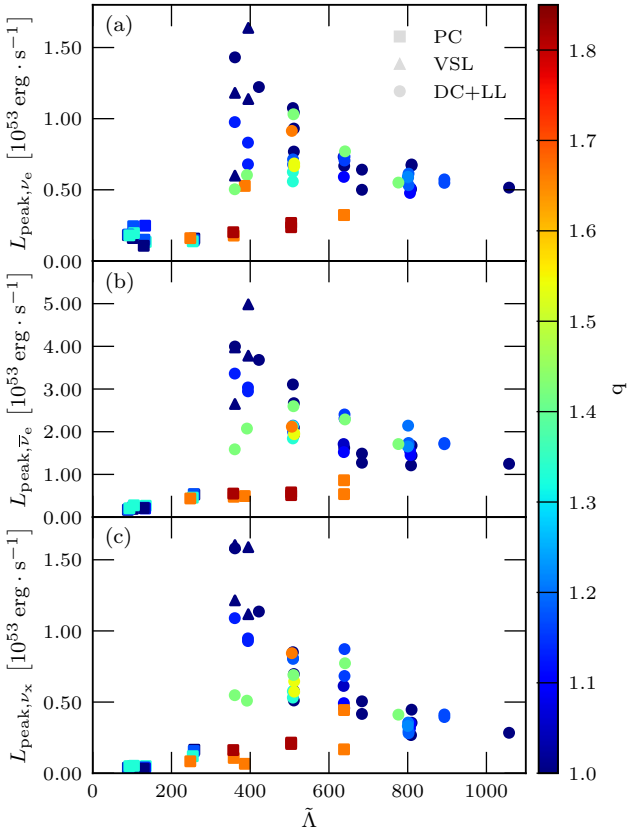

Fig. 2 Peak luminosity L_{peak} plotted against the reduced dimensionless tidal deformability $\tilde{\Lambda}$ for electron neutrinos (panel (a)), electron antineutrinos (b) and heavy lepton neutrinos (c). Colour indicates the BNS mass ratio. Note the different abscissa scales in the three panels.

4 Results

4.1 Luminosity peak and peak broadness

We start by exploring the peak luminosities for the different neutrino species. Fig. 2 displays the dependency of the peak luminosities on the tidal deformability and mass ratio of BNS models. The peak luminosities approximately span the range $1 \cdot 10^{52} - 5.5 \cdot 10^{53}$ erg s^{-1} for electron antineutrinos, while the other two flavours do not go beyond $\sim 1.7 \cdot 10^{53}$ erg s^{-1} even in the most extreme cases. As noted in Sec. 3.2, the extreme neutron richness and high temperatures of the MNS matter at this point in the binary evolution enhance the production of electron antineutrinos over other species, hence the differences in the peak strengths between them. However, within the observed ranges it can be noticed how the peak luminosity values follow very similar trends in different neutrino species. In fact, there appears to be a roughly constant factor of ~ 3 between ν_e and ν_x neutrinos with respect to $\bar{\nu}_e$ ones. This simi-

larity between the flavours can be understood by noting that the qualitative behaviour of neutrino emission in this phase is influenced more by the bulk dynamics of matter than the specifics of neutrino interaction.

Looking at different classes of simulations, we notice two different trends. The PC simulations have very low peak luminosities. For symmetric systems, this is likely due to two related phenomena. On one hand the merger remnant collapses essentially right after merger, shutting down the central engine responsible for the majority of neutrino emission. On the other hand a massive disc around the BH cannot form, since most of the matter is caught in the collapse. Therefore the luminosity peaks in equal mass PC simulations are likely due to emission from the contact interface right at merger, and so are up to six times lower than other models. While equal-mass PC simulations cluster at low values of $\tilde{\Lambda}$ (bottom lower part of Fig. 2), models with higher $\tilde{\Lambda}$ also can result in a prompt collapse, if their mass ratio q is high enough. With respect to q (and thus to $\tilde{\Lambda}$) we observe a slightly upward trend of the PC peak luminosities. This can be understood by noting that the lighter object is more easily tidally disrupted as q increases, allowing for a more massive disc that contributes to neutrino emission.

The remaining simulation categories show a different and much stronger dependence on $\tilde{\Lambda}$. Equal- or nearly equal-mass DC and LL models generally have higher peak luminosity than their asymmetric counterparts and the luminosity peak values present a downward trend with respect to $\tilde{\Lambda}$. Systems characterized by a higher tidal deformability contain less compact stars, which collide in a less violent fashion. Under these conditions, shock heating is less prominent and neutrino emission is correspondingly smaller. The largest peak luminosities are observed for $380 \lesssim \tilde{\Lambda} \lesssim 420$. Varying the mass ratio of the system modulates this trend and creates a second branch of points, because the tidal disruption of one of the two stars leads also to less violent coalescences. On the other hand this trend is not strictly monotonic with respect to the mass ratio, because increased tidal disruption also tends to increase the disc mass, which can then contribute to neutrino emission. This behaviour can be contrasted to the analogous one of the time-averaged neutrino luminosity, where both branches (the equal- and unequal-mass ones) show a much more well delineated trend with respect to $\tilde{\Lambda}$ (see Sec. 4.2). We additionally notice how the VSL simulations (which are only four and close to $q = 1$) provide a sort of transition between the $q \approx 1$ maximum of the DC+LL sample and the PC $q \approx 1$ branch.

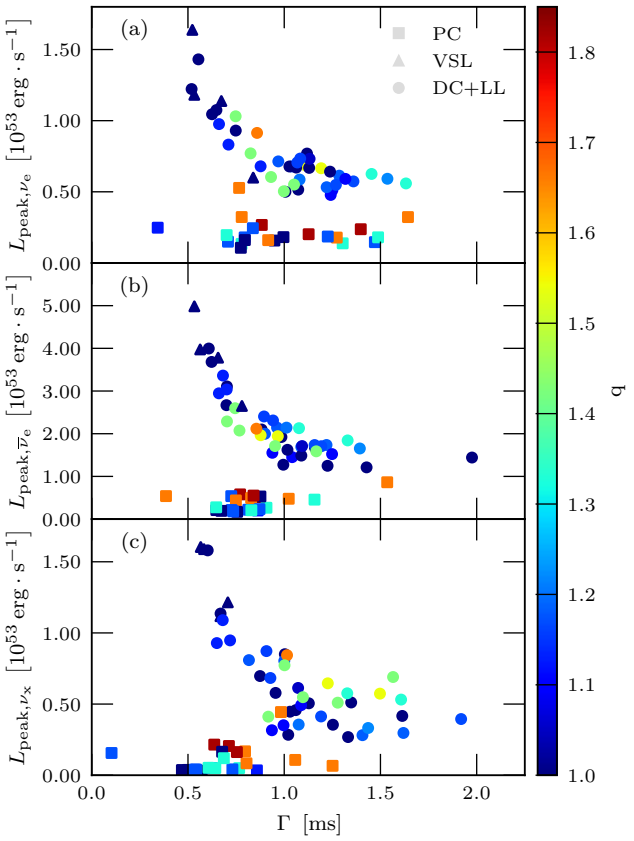

Fig. 3 Peak luminosity, L_{peak}, as a function of the FWHM of the peak, Γ, for electron neutrinos (panel (a)), electron antineutrinos (b) and heavy lepton neutrinos (c). Colour indicates the BNS mass ratio. Note the different abscissa scales in the three panels.

We then consider the broadness of the first peak of the neutrino luminosity. Fig. 3 presents the dependence of the peak luminosity L_{peak} to Γ, the FWHM of a Gaussian function fitted to the peak. In this case too we observe two distinct trends, one for the PC simulations and one for the other three categories. In the VSL, DC and LL simulations, as the peak luminosity decreases with increasing $\tilde{\Lambda}$, the peak broadness follows the inverse trend and increases. In part this increase (as the decrease of the peak values) can be related to the reduced compactness of stars showing higher deformability. In more compact systems, the outer layers of the stars are not very extended: the initial contact and temperature increase of these layers is shortly followed by the proper merger. On the other hand in more extended stars with higher deformability the contact and compression of these layers take longer. There is however a more quantitative and precise explanation. As noted in Sec. 3.2, the peaks of the neutrino luminosity arise as the results of shock waves generated by the oscillations of the merger remnant. The time scale of these

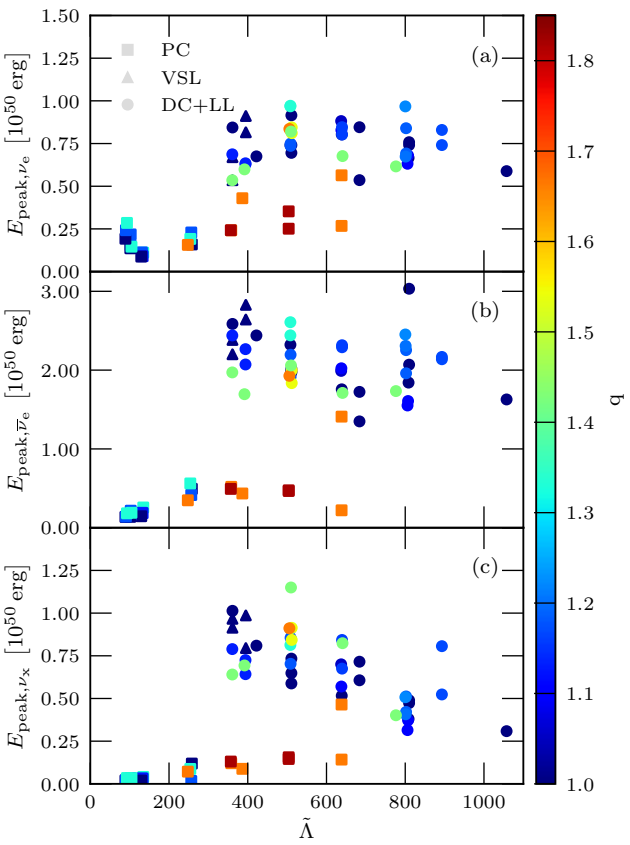

Fig. 4 Energy emitted by the peak E_{peak} as a function of the reduced dimensionless tidal parameter $\tilde{\Lambda}$ for electron neutrinos (panel (a)), electron antineutrinos (b) and heavy lepton neutrinos (c). Colour indicates the BNS mass ratio.

oscillations is ~ 1 ms and this is indeed the typical peak broadness: as shown in Fig. 3, Γ varies between 0.2 and 2 ms. However the time scale of oscillations is related to the free-fall time scale of the remnant, which scales as $t_{\mathrm{ff}} \propto \langle\rho\rangle^{-1/2}$, where $\langle\rho\rangle^{-1/2}$ is the mean density of the MNS. Since stars with higher deformability have generally lower $\langle\rho\rangle$, they show longer oscillations time scales, and this is reflected in the broadness Γ of the first neutrino luminosity peaks. This observation can be recast in a different way which is physically more meaningful. Note that in Fig. 3 it appears that for the VSL+DC+LL branch, L_{peak} and Γ are loosely inversely proportional to each other, so that their product is roughly constant. The expression:

$$E_{\mathrm{peak}} = \frac{1}{2}\sqrt{\frac{\pi}{\ln 2}}\, L_{\mathrm{peak}}\Gamma\,, \tag{16}$$

which is proportional to this product, is the time integral of the Gaussian we employed as fitting function and represents an estimate of the energy released by the first neutrino peak. We plot this quantity in Fig. 4. It is clear that E_{peak} is broadly constant, with typical values of $0.75\cdot10^{50}$ erg for ν_{e}'s and ν_{x}'s, and of $2.25\cdot10^{50}$ erg for $\bar{\nu}_{\mathrm{e}}$'s. Individual simulations scatter around these values with a maximum deviation of a factor of 2. This allows to provide a very concise characterization of the first neutrino luminosity peak: as long as the remnant does not collapse promptly after merger, the first luminosity peak releases a roughly constant amount of energy of $\approx 10^{50}$ erg. Finally, it is also clear from Fig. 3 and Fig. 4 that the arguments outlined above do not apply to PC simulations. The almost immediate collapse of the merger remnant means that not only L_{peak} is very low (as noted above), but also E_{peak}. Furthermore no time scale argument can apply to a collapsed remnant since it does not emit neutrinos. Indeed we see that while the typical values of Γ are the same for PC simulations, they do not appear to follow any particular trend with respect to either $\tilde{\Lambda}$ or q.

4.2 Time-averaged luminosities

Next we examine the average neutrino luminosity for different neutrino species, showed in Fig. 5 in dependence on the tidal deformability and mass ratio of BNS models. In this case the analysis is limited to the DC and LL simulations, since for the other two the average luminosity is not well defined. In this case the values span the range $0.6\cdot10^{53} - 1.4\cdot10^{53}$ erg s^{-1} for electron antineutrinos. The other two flavours mostly vary in the range $0.2\cdot10^{53} - 0.6\cdot10^{53}$ erg s^{-1}. Similarly to the peak luminosities, different neutrino species follow very similar trends, differing in this case too by a roughly constant factor between 2 and 2.5. The physical explanation of this trend outlined in the previous section applies in this case as well: the qualitative behaviour of neutrino emission is influenced more by the bulk dynamics of matter than by the specifics of neutrino interaction, while the extreme neutron richness of the system enhances the production of electron antineutrinos. The reduction of the scaling factor between the different flavours with respect to the first peak is due to the fact that the unbalanced $\bar{\nu}_{\mathrm{e}}$ emission leptonizes the remnant, partially reducing its own emission mechanism.

In order to corroborate these observations, we have considered the dependence of the average luminosities on each other, plotting each neutrino flavour against the other two. This is shown in Fig. 6. The figure clearly indicates the presence of a linear correlation between the average luminosities of any two flavours. While we refrain from fitting a straight line trough our data points, judging their quality too poor to warrant such an analysis, the correlation is evident. It can be seen that there

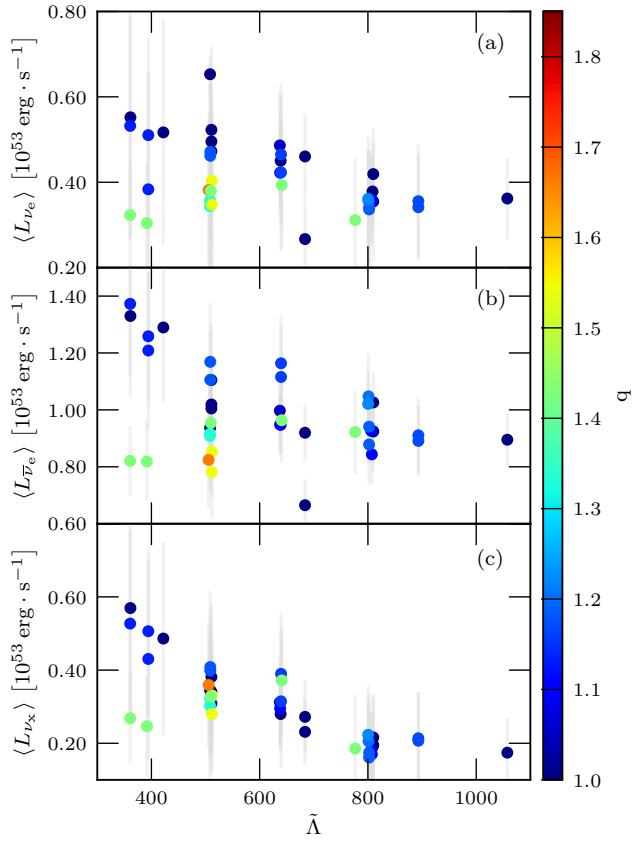

Fig. 5 Average luminosity $\langle L_\nu \rangle$ as a function of the reduced dimensionless tidal deformability $\tilde{\Lambda}$ for electron neutrinos (panel (a)), electron antineutrinos (b) and heavy lepton neutrinos (c) for DC and LL simulations. Colour indicates the BNS mass ratio while grey bars the standard deviation of the values.

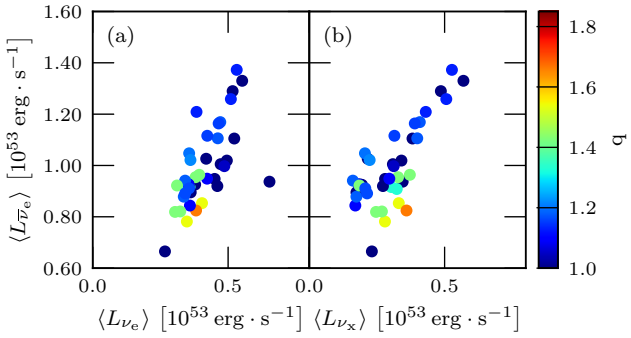

Fig. 6 Average luminosity $\langle L_\nu \rangle$ of two neutrino flavours plotted against each other for DC and LL simulations. Panel (a): $\langle L_{\bar{\nu}_e} \rangle$ vs. $\langle L_{\nu_e} \rangle$; panel (b): $\langle L_{\bar{\nu}_e} \rangle$ vs. $\langle L_{\nu_e} \rangle$. Colour indicates the BNS mass ratio.

is a proportionality factor of ~ 2.5 between the average luminosities of electron neutrinos and antineutrinos, and a slightly smaller coefficient between electron antineutrinos and heavy neutrinos.

Moving back to Fig. 5, equal-mass models values decrease with increasing tidal deformability. In this case too the explanation outlined in Sec. 4.1 holds true: higher tidal deformability leads to softer collisions with less shock heating, in turn leading to smaller neutrino emission. Also in this case varying the mass ratio creates a second branch, with generally smaller average luminosities than equal-mass binaries. While this second branch does not shows a monotonic dependence on $\tilde{\Lambda}$ in the case of peak luminosities (see the previous section), it is much more prominent in the case of average luminosities and our data suggests it is monotonically increasing with respect to $\tilde{\Lambda}$, at least for $\tilde{\Lambda} \lesssim 700$. This trend finds an explanation in the amount of matter tidally expelled from the NS at the time of merger[2]. In BNS systems characterized by high values of q, one of the two stars is tidally disrupted before and during the merger by the gravitational pull of the companion. In systems with higher $\tilde{\Lambda}$ the stars are less compact and a significant amount of matter is less strongly bound to the star. This matter will be expelled and increase in temperature, contributing to neutrino emission, thus explaining the upward trend.

The explanation of the differences between the peak and the average luminosities can be partially found in the act of taking a time average. Peak luminosities are by their definition associated to a transient and quite violent phase in the evolution of the system, the properties of which are dependent on several factors, and that cannot be satisfactorily described with a single parameter such as $\tilde{\Lambda}$ or q. Therefore it is to be expected for peak luminosities to show a larger variability. On the other hand, taking an average value can help to isolate a trend present in the data, which is revealed in Fig. 5. We can find further support for this line of reasoning by looking at the grey bars in Fig. 5. The bars represent the time variability of the data around the average values, represented by the points, as explained in Sec. 3.3. As can be seen the bars are quite wide, spanning a range that in some cases is as wide as the value of the average value to which they are associated: stated differently, the neutrino luminosities oscillate rather widely as a function of time around their averages. It is therefore

[2] In this context we are not exclusively talking about the so-called dynamical ejecta, i.e. matter which becomes gravitationally unbound due to tidal forces and shock heating and eventually leaves the system. We simply refer to the tidal tails of matter resulting from the disruption of one of the two NSs in the system, which is not part of the merger remnant. Part of this matter may become unbound and be ejected, but a significant portion will remain gravitationally bound and collect in an accretion disc.

evident that computing such averages is necessary to reveal meaningful relations in the data, which would otherwise present no appreciable correlation. Note that the origin of this variability is physical, being linked to e.g. the oscillations of the central object. Moreover their width also shows a trend with $\tilde{\Lambda}$: BNS mergers characterized by smaller $\tilde{\Lambda}$ and $q \approx 1$ present a more significant variability between the peaks and the valleys in the luminosity behaviour, reflecting the more violent dynamics of the merger.

Different resolutions and the inclusion or not of physical viscosity in the simulations do not seem to have a significant impact on the major results concerning the peak and average luminosities. A more detailed discussion about them is documented in Appendix A and Appendix B.

4.3 Long term behaviour of the luminosity

In order to better characterize the time evolution of the neutrino luminosity in the long term, we fit the data of a subset of simulations to a modified decaying exponential. We focus on LL remnants and only select simulations that extend further than 20 ms after merger, for a total of 10 simulations that last between 40 and 110 ms. We choose the simple model:

$$L_\nu(t) = L_{0,\nu} \exp\left(\frac{\alpha_\nu}{t} - \frac{t}{\beta_\nu}\right) \text{ for } \nu \in \nu_\mathrm{e}, \bar{\nu}_\mathrm{e}, \nu_\mathrm{x}\,, \qquad (17)$$

where $L_{0,\nu}$, $\alpha_\nu \geq 0$ and $\beta_\nu > 0$ are fitting constants, and fit it to the neutrino luminosity curves, starting from the time at which all neutrino flavours monotonically decrease until the end of the simulation. Eq. (17) is simply an exponential decay, augmented by the α-dependent term which allows for deviations from a purely decaying exponential at early times.

To measure the goodness of the fit, we first calculate the residuals between the actual luminosities and the fitted ones. We observe that the residuals can vary by up to 15% for heavy lepton neutrinos, and up to 10% for electron and antielectron neutrinos. We also observe that the largest residuals are observed at early times, when the luminosity is still characterized by small residual oscillations, around the transition to the decaying phase. We also estimate the coefficient of determination R^2 for all the models and the three neutrino species. In all the considered cases, its value is very close to 1.0, spanning from 0.93 for the heavy lepton neutrinos up to 0.99 for the electron neutrinos and antineutrinos. As it clearly appears from the values of R^2 and of the residuals, Eq. (17) is a good description of the long term evolution of neutrino luminosity.

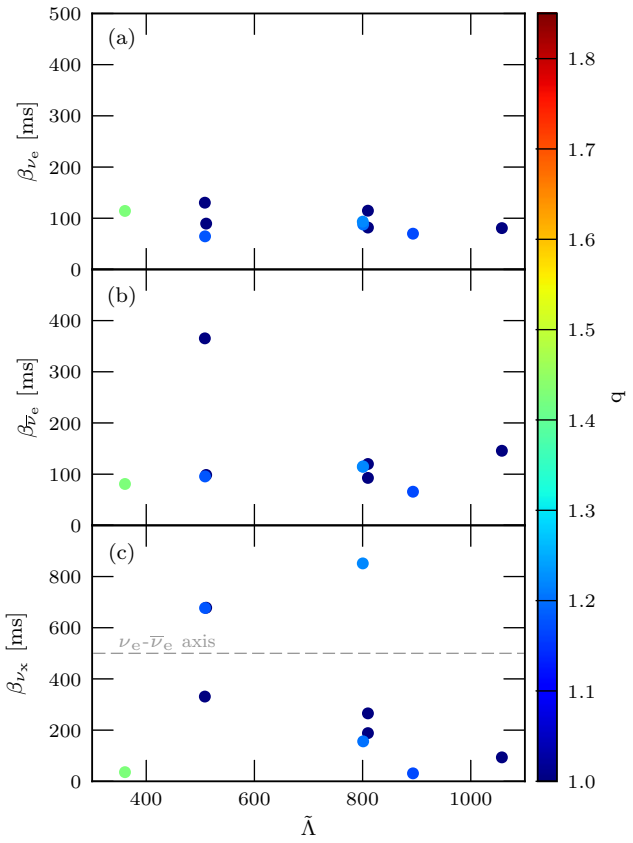

Fig. 7 Neutrino luminosity decay time scale β_ν as a function of the reduced dimensionless tidal deformability $\tilde{\Lambda}$ for electron neutrinos (panel (a)), electron antineutrinos (b) and heavy lepton neutrinos (c) for the longest LL simulations. Colour indicates the BNS mass ratio and the dashed line in panel (c) indicates the upper limit of the other two panels for ease of comparison.

We are interested in particular in the coefficients β_ν, which represents the time scale over which the luminosity drops. In Fig. 7 we present the values of β_ν for the three different species. While the value of this quantity does not seem to correlate strongly with either the reduced deformability $\tilde{\Lambda}$ or the mass ratio q, we can make a few interesting observations. The typical values of β_ν for electron neutrinos and antineutrinos are of the order of 100 ms. Barring a few outlying points, the corresponding value for heavy neutrinos is between 100 and 400 ms. It is interesting to see that these are rather long time scales, compared to the dynamical time scales associated with the MNS (~ 1 ms). Clearly the decline of neutrino emission reactions is a steady and relatively slow process, associated with the cooling of matter in the remnant and disc. Indeed, a time scale of several hundreds of milliseconds is more in line with both the cooling time scale of the MNS and with the accretion time scale of the disc [see e.g. 139, 141].

The difference in the decrease rate between ν_e's (or $\bar{\nu}_e$'s) and ν_x is likely related to the different production mechanisms and mean energies at the decoupling surfaces. Indeed a large fraction of the neutrino luminosity of all flavours comes from the cooling of the hot matter inside the MNS. However ν_x's decouple deeper inside the remnant and their spectrum is significantly harder (see Sec. 4.4). These hotter neutrinos still diffuse between the equilibrium decoupling surface and the last scattering surface, due to the opacity provided by quasi-elastic scattering off free baryons. Since the cross section for this process depends quadratically on the neutrino energy, the opacity for ν_x's (and consequently also its cooling time scale) is significantly larger and the cooling of the deepest layers proceeds at a slower pace.

If we extrapolated Eq. (17) to time scales longer than the accretion time scale ($\lesssim 1$ s, see for example [139]), the total emitted energy would be of the order of a few times 10^{52} erg, i.e. almost one order of magnitude smaller than expected. We speculate that this result points to the fact that the exponential decrease we observe is mostly due to the evolution of the accretion luminosity only. However, once a significant portion of the disc has been consumed, the luminosity coming from the cooling of the central object will take over and it will likely decrease with a different time scale. Indeed, to provide a total radiated energy of the order of 10^{53}erg, its decreasing pace is expected to be significantly slower and in line with its cooling time scale.

4.4 Time-averaged mean energies

The neutrino mean energies, averaged on the later part of DC and LL simulations, present a radically different behaviour compared to the luminosities described in the previous sections. In Fig. 8 we plot the averaged mean energies for all three neutrino species as a function of the reduced tidal deformability. The typical energy values are ~ 10 MeV, ~ 14 MeV and ~ 23 MeV for electron neutrinos, electron antineutrinos and heavy neutrinos, respectively (note that these are the same values reported in Ref. [61] and references therein). This hierarchy of energy values can be explained by relating it to the properties of the region where neutrino decoupling from the fluid occurs. In this case we are interested in the equilibrium surfaces, where neutrino energy spectra decouple from the fluid but are not yet free-streaming. It has been shown how in BNS mergers and for long-lived remnants these surfaces lie at increasing radii further away from the remnant for heavy neutrinos, electron antineutrinos and electron neutrinos, in this order. As temperature also decreases further away from the remnant, this explains the energy hierarchy between neutrino flavours [61]. Furthermore, it can be immediately seen that the grey bars, which represent the time variability of the mean energies around the average values plotted here (cf. Sec. 3.3), are extremely small, not being even visible in the leftmost two panels at this level of magnification. This shows that the neutrino mean energies can be considered constant in the early post merger phase. As noted in Sec. 3.2, this can be explained by noting that the thermodynamic conditions of matter at the surface of neutrino decoupling are constant in time in the later part of the evolution, since the location of the neutrinosphere itself does not evolve significantly at this point [61]. A similar observation also explains why the neutrino mean energies are the same, within a flavour, regardless of the masses or EOS of the BNS model (note the constant trend with respect to $\tilde{\Lambda}$ and q in Fig. 8). The thermodynamics condition at the neutrinosphere are not only constant in time, but owing to the rather large radii of the neutrinospheres themselves (~ 20 km), they are also rather insensitive to variations in the bulk dynamics of the system driven by the initial conditions. We speculate that this could result from two main reasons. One the one hand, since the location of the equilibrium decoupling surface depends at leading order on the matter density, it is likely that the properties of the accretion disc (and in particular of the density-temperature profile) are rather independent from the specific binary system, especially once the disc has reached a quasi-stationary state and a high degree of axisymmetry. On the other hand, matter temperature also influences the neutrino opacity, mostly through the energy of the diffusion thermal neutrinos. If a disc is hotter (e.g. because it was formed in a more violent collision), the larger temperatures increase the opacity inside the disc, moving the decoupling surfaces at larger radii and, thus, lower temperatures. Clearly, these two effects tends to compensate each other, providing similar decoupling temperatures in all cases.

5 Discussion

5.1 Comparison with GW luminosities

Neutrinos provide the most relevant radiation loss from merging BNSs on the cooling time scale of the remnant. However, the inspiral and the early post-merger phase ($\lesssim 20$ ms) are GW-dominated [142]. In Fig. 9 we present a comparison between the GW and total neutrino peak luminosities for all simulations presented in this work. The former are computed as the first peak that the GW luminosity reaches during the merger and subsequent dynamical phase. Usually, $L_{\rm peak,GW}$ are between one and three orders of magnitude larger than

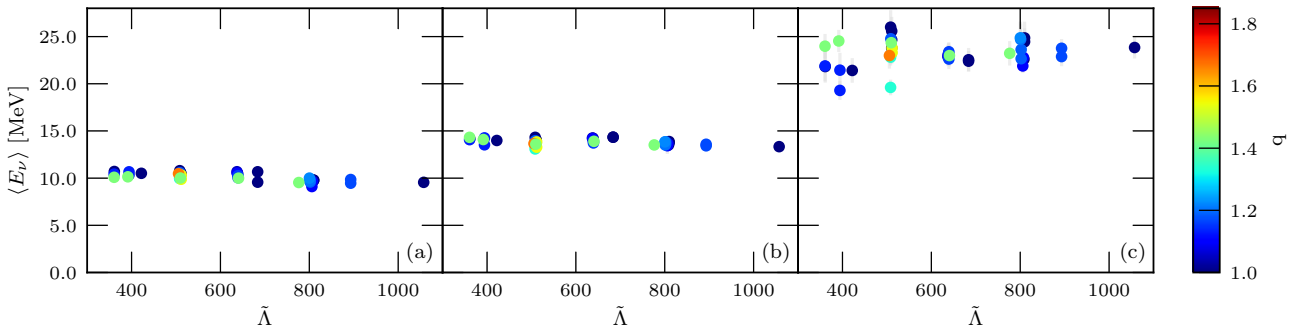

Fig. 8 Neutrino average mean energy $\langle E_\nu \rangle$ plotted against the reduced tidal deformability $\tilde{\Lambda}$ for electron neutrinos (panel (a)), electron antineutrinos (b) and heavy lepton neutrinos (c) for DC and LL simulations. Grey bars indicate the standard deviation in time from the average value.

$L_{\mathrm{peak},\nu}$. More specifically, we can recognize three different regimes. For VSL, DC and LL systems for which $q \gtrsim 1$, there is a correlation between the luminosity in GWs and ν's at peak. This is due to the fact that neutrino radiation is emitted by the same matter that produces also the GW emission, once it has been heated up by the collision. Since the binary properties that boost the GW emission [see, e.g. 143] are the same ones that increase the remnant temperature (see Sec. 3.2, Sec. 4.1 and Sec. 4.2), the two luminosities increase together. If the mass ratio becomes significantly different from 1, $\tilde{\Lambda}$ decreases and both $L_{\mathrm{peak,GW}}$ and $L_{\mathrm{peak},\nu}$ decrease, but the reduction in GWs is more significant. This is due to the fact that the strong-field dynamics behaviour for $L_{\mathrm{GW,peak}}$ is not precisely captured by $\tilde{\Lambda}$, but by the so-called κ_2^L parameter, which is a different linear combination of the tidal polarizability coefficients weighted by a function of the the mass ratio and of the total mass of the system, see [143]. In particular, κ_2^L is the perturbative parameter that enters the 5th order post-Newtonian term related to the tidal effects in the binary evolution. Finally, in the PC cases the two luminosities follow opposite trends: GW emission is the brightest for PCs resulting from symmetric BNSs merger, but these are the systems for which $L_{\mathrm{peak},\nu}$ is the lowest. This is due to the fact that the GW peak happens around merger, while matter disappears inside the BH horizon immediately after it, without contributing to the neutrino emission. This effect is partially mitigated by the tidal disruption of the secondary happening in the high-q cases.

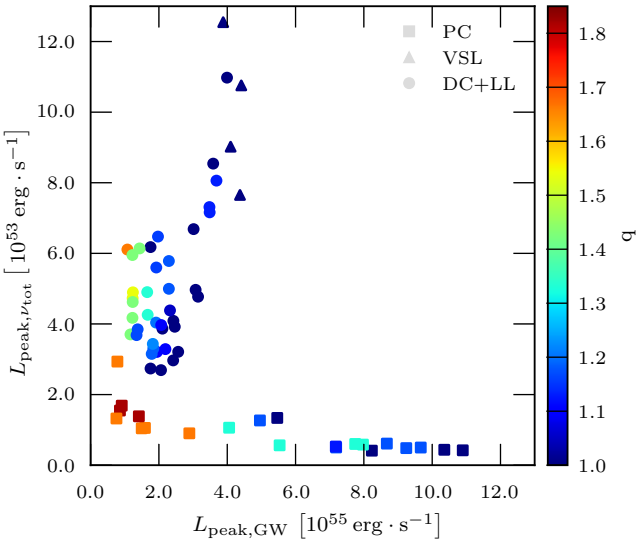

Fig. 9 Neutrino peak luminosity $L_{\nu,\mathrm{peak}}$ as a function GW peak luminosity $L_{\mathrm{GW,peak}}$. Colour indicates the BNS mass ratio.

5.2 Influence on the electron fraction and kilonova colour

In addition to being a primary source of cooling, neutrinos can change the electron fraction, Y_e, of matter through charged current reactions, including electron, positron, ν_e and $\bar{\nu}_\mathrm{e}$ captures on free neutrons and protons. All these reactions are relevant inside the neutrino surfaces to change Y_e from cold, neutrino-less, β-equilibrium conditions ($Y_\mathrm{e} \sim 0.05$ for the relevant densities) to finite temperature, neutrino trapped equilibrium conditions. In the following, we will assume that the net effect is an increase in Y_e from ~ 0.05 to 0.15. Since the luminosities we are considering in this work represent the radiation streaming freely outside the neutrino surfaces, in the following we estimate the further effect of the absorption of electron neutrinos and antineutrinos on Y_e for a fluid element that is ejected from the BNS, while we neglect the residual impact of electron and positron captures (this approximation is valid as long as the temperature in the ejecta expand-

ing outside the neutrino surfaces is below a few MeV [144]).

We assume a (simplified) model for the evolution of the $\nu_{\rm e}$ and $\bar{\nu}_{\rm e}$ luminosities. In particular, for $\bar{\nu}_{\rm e}$'s we have:

$$L_{\bar{\nu}_{\rm e}}(t) = \begin{cases} \langle L_{\bar{\nu}_{\rm e}} \rangle & 0 < t < 10{\rm ms} \\ \langle L_{\bar{\nu}_{\rm e}} \rangle \exp\left(-\frac{t-10{\rm ms}}{\beta_\nu}\right) & t \geq 10{\rm ms}\,, \end{cases} \tag{18}$$

where $\langle L_{\bar{\nu}_{\rm e}} \rangle$ is the average peak luminosity presented in Sec. 4.2 and t the time after the escape of the fluid element from the neutrino surface, while we set $\beta_{\bar{\nu}_{\rm e}} = 100\,{\rm ms}$, based on Fig. 7. For $\nu_{\rm e}$'s we assume:

$$L_{\nu_{\rm e}}(t) = \begin{cases} \langle L_{\nu_{\rm e}} \rangle & 0 < t < t_{\nu_{\rm e}} \\ \langle L_{\nu_{\rm e}} \rangle \exp\left(-\frac{t-t_{\nu_{\rm e}}}{\beta_\nu}\right) & t \geq t_{\nu_{\rm e}}\,, \end{cases} \tag{19}$$

which is analogue to the one for $\bar{\nu}_{\rm e}$, but in which $t_{\nu_{\rm e}}$ is fixed by the condition:

$$L_{\nu_{\rm e}}(t_{\nu_{\rm e}}) = L_{\bar{\nu}_{\rm e}}(t_{\nu_{\rm e}})\,, \tag{20}$$

meaning that the two luminosities are the same on the time scale set by β_ν, as visible in the long term evolution of our LL models. In practice this results in $t_{\nu_{\rm e}}$ being given by:

$$t_{\nu_{\rm e}} = 10\,{\rm ms} - \beta_\nu \log\left(\frac{\langle L_{\nu_{\rm e}} \rangle}{\langle L_{\bar{\nu}_{\rm e}} \rangle}\right)\,, \tag{21}$$

and having typical values of $\approx 100\,{\rm ms}$. We further consider constant mean energies, equal to the average ones extracted from the simulations and presented in Sec. 4.4. We compute the evolution of $Y_{\rm e}$ based on the equation:

$$\frac{{\rm d}Y_e}{{\rm d}t} = \lambda_{\nu_{\rm e}}(1 - Y_{\rm e}) - \lambda_{\bar{\nu}_{\rm e}} Y_{\rm e}\,, \tag{22}$$

where $\lambda_{\nu_{\rm e}}$ and $\lambda_{\bar{\nu}_{\rm e}}$ are the $\nu_{\rm e}$ and $\bar{\nu}_{\rm e}$ capture rates, respectively, with the initial condition $Y_{\rm e}(t=0) = 0.15$. The expressions of $\lambda_{\nu_{\rm e}}$ and $\lambda_{\bar{\nu}_{\rm e}}$ are taken from equations (C.4)-(C.10) and (3) of [145]. In particular, from equation (3) it is clear that the neutrino flux depends on the radial distance and from its evolution. We consider $R(t) = vt + R_0$ where R_0 is the typical radial distance of the neutrino surface and v the ejecta speed. We further know that neutrino emission is not isotropic, due to the shadow effect provided by dense matter in the disc along the equatorial plane. We then consider two possible directions identified by the polar angle θ, namely $\theta = 0$ (polar direction) $\theta = \pi/2$ (orbital plane), and the angular dependence implied by equation (3) in [145], assuming $\alpha = 2$, which corresponds to a polar flux three times larger than the equatorial one.

We consider two kinds of ejecta: the dynamical and the disc wind ejecta. The dynamical ejecta [see e.g. 146, 147, 148, 106, 149, 150, 151, 152, 75, 98, 153, 154, 58, 155, 88, 156, 157, 135, 80] are the matter expelled within a few dynamical time scales after merger ($\lesssim 5\,{\rm ms}$), with typical average speeds ranging between 0.1-0.3c, by tidal torques and shock waves propagating inside the remnant. We compute the speed of the ejecta as a function of $\tilde{\Lambda}$ and q, based on the fitting formula equation (6) presented in [60], using in particular results from the `MORefSet` dataset. Disc winds [see e.g. 50, 158, 159, 141, 160, 161, 55, 139, 56, 162, 163, 164, 165, 134, 57, 166, 167, 168, 169, 170] are possibly expelled on the disc evolution time scale ($\sim$ 10ms - 1s) by a variety of mechanisms, including neutrino absorption itself, nuclear recombination following viscous spreading of the disc, spiral wave triggered by long-standing $m = 1$ bar modes in the remnant, magnetic processes. In this case, the ejection speed is expected to be $\sim 0.05 - 0.1\ c$. In our calculation, we consider a representative value of $v = 0.08c$ [3]. For the ejecta expelled in the orbital plane we assume $R_0 = 20\,{\rm km}$, corresponding to the typical radius of the most relevant $\nu_{\rm e}$ and $\bar{\nu}_{\rm e}$ neutrino surfaces inside the disc [61]. For the ejecta expelled along the polar axis, we consider $R_0 = 15\,{\rm km}$, corresponding to the radius of MNS.

In Fig. 10, we present the final results of our $Y_{\rm e}$ calculations (i.e., at 1 second after merger) taking into account only LL simulations. In the top (bottom) panels, we collect results for the dynamical (wind) ejecta, while in the left (right) panels, along the polar axis (equatorial plane). The gray triangles mark the equilibrium $Y_{\rm e}$, $Y_{\rm e,eq}$, defined as the value of $Y_{\rm e}$ obtained by assuming ${\rm d}Y_e/{\rm d}t = 0$ in Eq. (22) and no evolution of the radius [see e.g. 144]. In practice, it is the value of the electron fraction that the fluid element would reach if the dynamical time scales were significantly smaller than the expansion time scales. In our case, it represents the asymptotic limit of our calculations. We observe that $0.28 \lesssim Y_{\rm e,eq} \lesssim 0.38$, without any clear trends with $\tilde{\Lambda}$. Due to the fast expansion, the final $Y_{\rm e}$ computed by integrating Eq. (22) is smaller that $Y_{\rm e,eq}$. Since the expansion speed is larger for the dynamical ejecta than for the disc wind ejecta, the final $Y_{\rm e}$ is usually $\lesssim 15\%$ smaller for the former, since the larger initial luminosity is not enough to compensate the fast expansion. Additionally, the different flux intensities produce an appreciable difference between the polar and the equatorial directions. The difference is here more pronounced ($\sim 20\%$). In all cases, there is a trend both with respect to $\tilde{\Lambda}$ and q: the change in $Y_{\rm e}$ is smaller for more deformed BNSs and for more asymmetric binaries: this is consistent with the

[3] Magnetically-driven and spiral wave winds could be characterized by larger speeds, closer to the ones of dynamical ejecta, see e.g. [165, 134, 135].

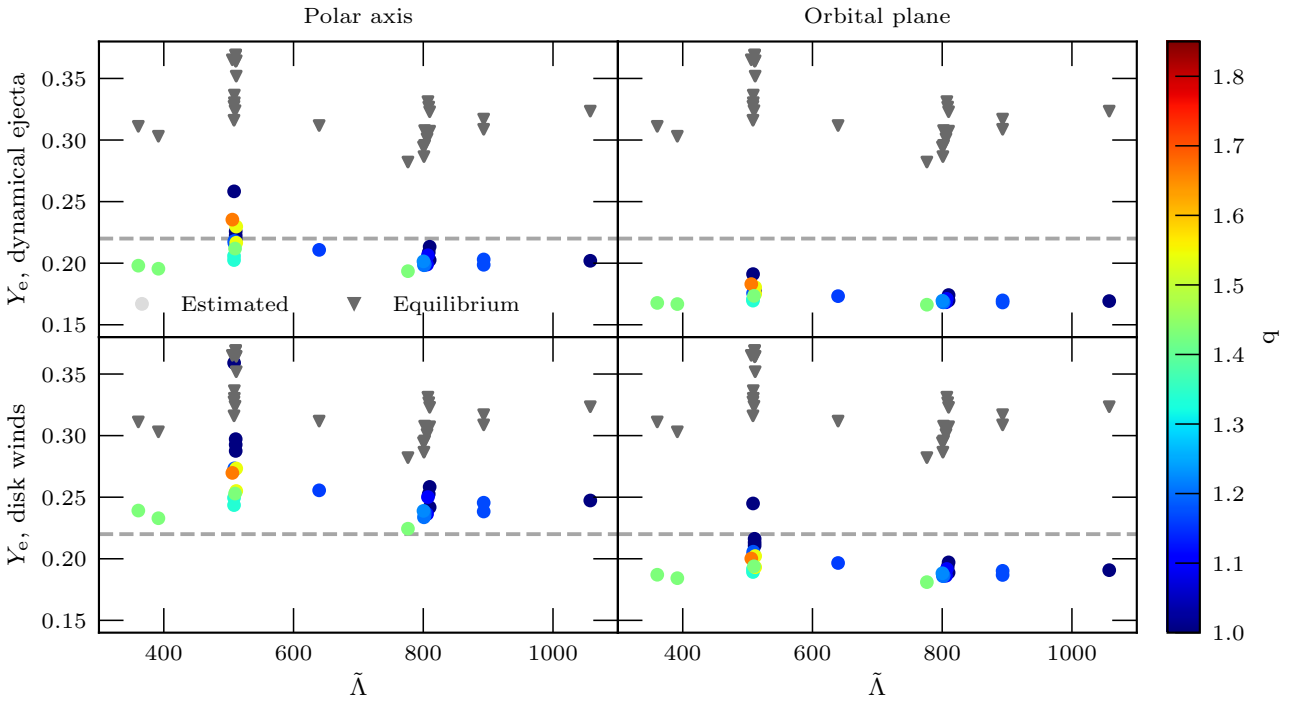

Fig. 10 Estimated electron fraction Y_e of an ejected fluid element as a function of the reduced tidal deformability $\tilde{\Lambda}$ for dynamical ejecta along the polar axis (top left panel) and orbital plane (top right), and for a disc wind along the polar axis (bottom left) and orbital plane (bottom right) for LL simulations. Colours indicate the BNS mass ratio while dashed lines indicate the threshold between strong and weak r-process nucleosynthesis ($Y_e = 0.22$). The grey triangles represent, for each simulation, the corresponding equilibrium Y_e. See the text for more details.

variation of the luminosities observed in Sec. 4. We notice that the initial condition $Y_e(t = 0) = 0.15$ is underestimated in the case of dynamical, polar ejecta, where simulations indicate $Y_e \approx 0.2$ immediately outside from the neutrino surface. This means that in that case our final Y_e should be intended as a lower limit. While appropriate to study general and robust trends, we stress that a detailed evolution requires to extract Y_e from the simulations. We notice, however, that our results are in good qualitative agreement with simulations results. In particular, the polar irradiation is effective in increasing Y_e is all possible configurations, due to the larger expansion time scale. By comparing the values of Y_e in the different cases and with the equilibrium one, we can however conclude that the dependence on the final Y_e on $\tilde{\Lambda}$ and q is rather weak.

Additionally, in Fig. 10 we highlight $Y_e = 0.22$, corresponding to the value of Y_e above which strong r-process nucleosynthesis is inhibited. Ejecta with an electron fraction above or around this value is more prone to power a blue kilonova, while for the ejecta whose electron fraction is below that value the production of lanthanides and actinides provides larger opacities to photons, resulting in a redder kilonova peaking at later times. Our results confirm previous findings: equatorial ejecta tend to produce red kilonovae in all configurations, while polar dynamical ejecta produced in equal mass and more compact mergers blue ones.

5.3 Comparison with previous results

The major outcomes of our work are in good qualitative agreement with previous works. For example, a comparison between the neutrino luminosities produced by BNS mergers with different masses and/or different EOSs in Numerical Relativity was carried out in Refs. [75, 154, 76]. The reported qualitative behaviours are similar to what we find, with peak luminosities of the order of several 10^{53} erg s^{-1}, dominant $\bar{\nu}_e$ emission, and an oscillatory phase lasting 10-15 ms post merger followed by a slow decay. As in our analysis, the softer SFHo EOS (resulting in smaller $\tilde{\Lambda}$'s) provides systematically larger luminosities. A relevant difference is the relative importance between ν_e's and ν_x's, whose luminosities are comparable in our simulations and in simulations from Ref.[76], while ν_e luminosities from Ref. [75, 154] are smaller but closer to the $\bar{\nu}_e$ ones. This difference is likely related to the different implementation details of the neutrino treatment.

Compared with Newtonian simulations, as for example the ones presented in Ref. [47, 62, 151], we see again a qualitative agreement, but some quantitative differences. In these cases, the lower neutrino luminosities were probably a consequence of the lower remnant temperature observed in the less violent merger dynamics that characterize Newtonian gravity simulations employing stiff EOSs. It is interesting to note that values of the luminosities intermediate between ours and the ones obtained in Newtonian simulations were obtained in Ref. [79], using a Smoothed Particle Hydrodynamics code with conformally flat spacetime approximation coupled with a leakage scheme. The duration of the oscillatory phase were in these models also shorter than ours, probably resulting from a possibly different post merger dynamics of the remnant. However, the hierarchy and the numerical values of the mean energies were very compatible with ours and rather independent on the BNS properties. Also the relative importance of $\nu_{\rm e}$ and $\nu_{\rm x}$ is closer to our results. Finally, we compare our results with the ones reported in [58] for a light BNS merger (1.2-1.2 $M_{\odot}$) employing the LS220 EOS. The rather low luminosities obtained in this case are in overall agreement with the fact that such a system is characterized by a relatively large value of $\tilde{\Lambda}$. $\nu_{\rm x}$ luminosities are however more relevant here than in our results. This difference is partially explained by the larger $\langle E_{\nu_{\rm x}} \rangle$ obtained in that analysis. A more important difference is represented by the different evolution of the luminosities with time. While also in this case one can see fast oscillations in all neutrino luminosities on the dynamical time scale, the presence of a strong peak in the very first post-merger phase is not present in these simulations. On the contrary, all luminosities tend to increase up to the end of the simulation. The relatively short duration of the simulation and the need of considering the neutrino time of flight make the comparison harder in this case.

5.4 Limitations of the present analysis

It is important to note the few limitations that affect the present analysis. First of all, since the data we work on has been generated by numerical simulations, the usual caveats that apply in this context apply in our case as well, namely the loss of accuracy due to finite resolution and the difficulty of obtaining proper convergence in the post-merger phase. In addition, a more serious limitation concerns the algorithms for neutrino transport that we rely on. They attempt to strike a balance between computational cost and physical realism, but in doing so neglect some of the finer details of neutrino dynamics. One such example is the assumption of purely radial propagation of neutrinos in the M0 scheme, which only approximately reflects the complex geometry of BNS systems. Moreover, a grey NLS is not a proper transport scheme, since it only approximates the diffusion regime through time scale arguments. A detailed comparison between different neutrino treatments in the context of CCSNs and BNS mergers [e.g. 50, 171, 172, 173, 174, 175, 72] recently addressed the problem of the accuracy of approximated neutrino transport scheme in astrophysical environments. The overall outcome is that, while well gauged leakage schemes can still provide a qualitatively correct picture, quantitative statement suffers from an error usually of the order of $20-30\%$. While this analysis could be robustly grounded on detailed models in the context of CCSNs, neutrino modelling in BNS mergers is less mature. The non-trivial angular dependence also introduces an additional uncertainties. Because of these reasons, we have decided to focus mostly on peak and integrated quantities, stressing in particular trends with respect to global binary properties and to the neutrino flavours.

Furthermore the neutrino treatment employed in this work uses what we think is the minimal set of neutrino-matter reactions necessary to account for in BNS merger scenarios, both in terms or reactions and reaction rate implementations. However a detailed analysis of the role and impact of these and other missing reactions is presently lacking. One of the main reason is that the large uncertainties that still plague neutrino transport in BNS merger simulations do not allow to robustly address this problem. In parallel to the improvement of transport schemes, it would be desirable also to improve the level of microphysics in the simulations, for example by extending the set of reactions and by implementing more detailed reactions rates and opacities, more consistent with nuclear matter properties [see e.g. 176, 177, 178].

Finally, neutrinos are expected to undergo flavour conversions due to their small, but non-zero, masses. Neutrino oscillations will occur for the neutrinos emitted during and after a BNS merger. These oscillations will certainly happen in vacuum and due to matter interaction, in both cases relatively far from the merger remnant. However, collective and resonant neutrino oscillations could also happen closer to the neutrino surfaces and above the remnant [see e.g. 179, 180, 181, 182, 183]. These effects are not included in our simulation setup, but since we are mainly interested in characterizing the energy loss from the remnant this should not be a major limitation. The possible impact on the ejecta composition and on the neutrino-antineutrino annihilation is possibly more relevant and requires dedicated

studies, that at the moment are usually done in a post-processing fashion [184, 78, 79].

6 Conclusions

In this paper, we have analysed the behaviour of the neutrino luminosities and mean energies produced in the merger of two NSs and during the first tens of ms after it. We have considered the outcome of 66 BNS merger simulations in Numerical Relativity, exploring 51 distinct models. The various models differ because of the masses of the binary constituents and the employed NS EOS. Each model can correspond to multiple simulations due to the inclusion of viscosity of physical origin and because of the numerical grid's resolution. The simulation sample is homogeneous in terms of numerical setup and all simulations include neutrino emission through a grey neutrino leakage scheme [64] coupled to an M0 scheme for the propagation of neutrino radiation in optically thin conditions [98].

Despite the large variety of conditions, we found that the behaviour of the neutrino luminosities presents qualitative similarities, mostly depending on the fate of the remnant. Assuming that the central remnant does not collapse to a BH within the first 20 ms after merger (i.e. DC and LL cases in our classification), the early post merger phase is characterized by an intense neutrino emission (with total luminosities in excess of several times $10^{53}\,\mathrm{erg\ s^{-1}}$), showing a more pronounced first peak (usually occurring within the first 2-3 ms after merger), followed by ample oscillations whose period is comparable to the dynamical time scale of the merger remnant. After 10-15 ms, the oscillations subside and the luminosities enter an exponentially decreasing phase.

The bulk properties of the remnant, and in particular the matter temperature, determine the intensity of the emission. More symmetric and compact BNSs, resulting in more violent mergers and hotter remnants, have larger luminosities. The formation of shock waves produced by the bouncing central MNS and their propagation through the remnant up to the neutrino surfaces produce this characteristic peak structure. We additionally find that, unless the merger results in a PC, the neutrino luminosity correlates with the GW luminosities, since they both are enhanced by the same BNS properties.

Neutrinos come both from the cooling of the optically thick central MNS and from the innermost part of the accretion disc. The formation of a BH in the centre removes not only the MNS, but also a significant fraction of the disc. Then neutrino luminosities are significantly reduced when a BH forms. If the gravitational collapse happens within the first 5 ms (VSL simulations), only the first peak is present. If it happens promptly, i.e. without the formation of a MNS (PC simulations), only a weak and broad peak is observed.

We then studied the dependence of both the peak and average luminosity (where the latter is computed over the oscillatory phase) on the reduced tidal deformability parameter $\tilde{\Lambda}$. We found that for equal or nearly equal BNS mergers that do not collapse too quickly to a BH (i.e. LL and DC cases), the luminosity significantly increases (up to a factor of 3) as $\tilde{\Lambda}$ decreases, down to $\tilde{\Lambda} \approx 380$. BNS mergers characterized by similar $\tilde{\Lambda}$, but with mass ratios significantly different from 1 produce a less intense neutrino emission, due to the less violent nature of the tidally dominated merger dynamics. Prompt-collapse cases populate the low-$\tilde{\Lambda}$, low-L_ν portion of the result space, with an increasing trend in both quantities for more asymmetric binaries.

We additionally focused on the main luminosity peak. We found that, once the PC cases are excluded, in all cases the peak intensity anti-correlates with the peak width Γ: stronger peaks last less than weaker ones. Indeed, the energy emitted by this peak, $E_{\rm peak} \sim L_{\nu,{\rm peak}}\Gamma$ does not show any clear trend for non-PC models.

All the trends described above apply to all modelled neutrino species, i.e. $\nu_{\rm e}$, $\bar{\nu}_{\rm e}$, and $\nu_{\rm x}$, the latter being a collective species for heavy flavour (anti)neutrinos. Due to the neutron richness of the system and to the tendency of neutron rich matter to leptonize when decompressed and heated up, $\bar{\nu}_{\rm e}$ emission dominates over $\nu_{\rm e}$ and $\nu_{\rm x}$, at least during the early post-merger phase. In particular, $L_{{\rm peak},\bar{\nu}_{\rm e}} \sim 3L_{{\rm peak},\nu_{\rm e}}$ and $L_{{\rm peak},\nu_{\rm e}} \sim L_{{\rm peak},\nu_{\rm x}}$. Similar relations hold for the luminosity averaged over the first 10 ms, even if $\langle L_{\bar{\nu}_{\rm e}}\rangle/\langle L_{\nu_{\rm e}}\rangle \sim 2-2.5$. The reduction of the difference between the $\nu_{\rm e}$ and $\bar{\nu}_{\rm e}$ luminosities becomes more evident at later times, during the steadily declining phase, as a consequence of the early remnant leptonization, driving its neutron-to-proton content towards a new equilibrium.

Finally, we investigated the value of the neutrino mean energies and their dependence on the BNS parameters. We found that $\langle E_\nu\rangle$ is the least sensitive quantity, for all neutrino flavours, with $\langle E_{\nu_{\rm e}}\rangle \approx 10\,\mathrm{MeV}$, $\langle E_{\bar{\nu}_{\rm e}}\rangle \approx 14-15\,\mathrm{MeV}$ and $\langle E_{\nu_{\rm x}}\rangle \approx 20-25\,\mathrm{MeV}$. This hierarchy can be easily explained in terms of the different location of the neutrino surfaces [61].

Building on a simplified, yet physically motivated model for the neutrino luminosities based on our results, we have studied the potential impact of neutrino irradiation on the electron fraction of the matter expelled from a BNS merger. Our results agree with pre-

vious findings: for example, Y_e increases more significantly due to ν_e absorption in the polar direction and for slower disc winds. We further found that the range in luminosities has a weaker effect than the expansion time scale and the remnant geometry.

The major strengths of this work are the wide sample of models we employed and their relative homogeneity in terms of numerical setup. They qualify it as the first systematic study of the properties of the neutrino emission over a wide sample of BNS models available at present. As mentioned in Sec. 5.4, there are a few areas in which our approach could be improved. Yet we believe that the results presented in this work are relevant and possibly very useful. This stems chiefly from two considerations. First of all, while obtaining more precise, accurate and realistic data is indeed desirable, it is important to start building a phenomenological and theoretical picture from the data as they are available at present. Secondly, while more realistic neutrino treatments and overall improvements in simulation machinery will undoubtedly provide quantitative corrections to the data we collected and presented here, we believe that our approach captures the fundamental aspects of neutrino emission in BNS mergers. Moreover, our characterization of neutrino emission will likely work and find usefulness also as a reference point, to gauge the accuracy, performance and overall behaviour of the aforementioned advanced schemes.

Our analysis could also serve as input to study the detectability of neutrinos produced in a BNS merger [see e.g. 153]. Due to their small cross sections, it will be impossible to detect thermal MeV-neutrinos produced by a merger at the typical distance of several tens of Mpc (or even more) we usually expect to observe them. However, in the very unlikely case of a Galactic BNS merger, Hyper-Kamiokande [185] will be able to detect several tens of thousands neutrinos, similar to the case of a CCSN or even larger due to the larger neutrino luminosities, especially for $\bar{\nu}_e$'s. A BNS merger occurring in the outer skirt of our Galaxy (where it is more plausible to happen rather than inside the Galactic disc) will still result in a few thousands events. A handful of neutrinos could possibly be detected also if the merger happens in a nearly galaxy, up to a distance of a few times 10^3kpc. Our analysis could also be expanded towards the study of the spatial dependence of neutrino emission, as well as the its late post-merger properties, These information will be key to study, for example, the role of neutrino flavor conversions. However we leave these topics for future works.

Acknowledgements We thank the European COST Action CA16214 PHAROS "The multi- messenger physics and astrophysics of neutron stars" for the useful and stimulating discussions that have inspired this work, and the `CoRe` collaboration for providing simulation data. MC, AP and SB acknowledge the INFN for the usage of computing and storage resources through the `tullio` cluster in Turin. AP acknowledges the usage of computer resources under a CINECA-INFN agreement (allocation INF20_teongrav and INF21_teongrav). He also acknowledge PRACE for awarding him access to Joliot-Curie at GENCI@CEA. SB acknowledges funding from the EU H2020 under ERC Starting Grant, no.BinGraSp-714626, and from the Deutsche Forschungsgemeinschaft, DFG, project MEMI number BE 6301/2-1. DR acknowledges funding from the U.S. Department of Energy, Office of Science, Division of Nuclear Physics under Award Number(s) DE-SC0021177 and from the National Science Foundation under Grants No. PHY-2011725, PHY-2020275, PHY-2116686, and AST-2108467. NR simulations were performed on SuperMUC-LRZ (Gauss project pn56zo), Marconi-CINECA (ISCRA-B project HP10BMHFQQ, INF20_teongrav and INF21_teongrav allocation); Bridges, Comet, Stampede2 (NSF XSEDE allocation TG-PHY160025), NSF/NCSA Blue Waters (NSF AWD-1811236), Joliot-Curie at GENCI@CEA (PRACE-ra5202) supercomputers. This research used resources of the National Energy Research Scientific Computing Center, a DOE Office of Science User Facility supported by the Office of Science of the U.S. Department of Energy under Contract No. DE-AC02-05CH11231.

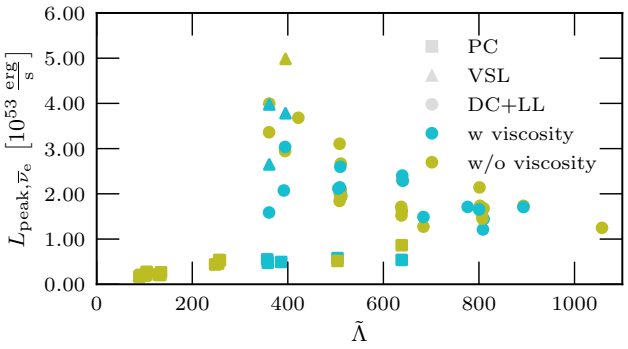

Fig. 11 Same as the middle panel of Fig. 2, but distinguishing simulations which take into account the fluid viscosity by means of the GRLES method from those that do not.

Appendix A: Influence of viscosity treatment

As mentioned in Sec. 2.3.3 and Sec. 3.1, part of our simulation sample employs an implementation of the GRLES method to effectively model the viscosity that results from the amplification of magnetic fields and the magneto-rotational instability (MRI) in the post-merger. In this appendix, we explore the impact that the inclusion or lack of viscosity has on the properties of neutrino emission. To this end Figs. 11, 12 and 13 present the same data that has been analysed in Secs. 4.1, 4.2 and 4.4, but separating the simulations employing the GRLES technique from those that do not employ it.

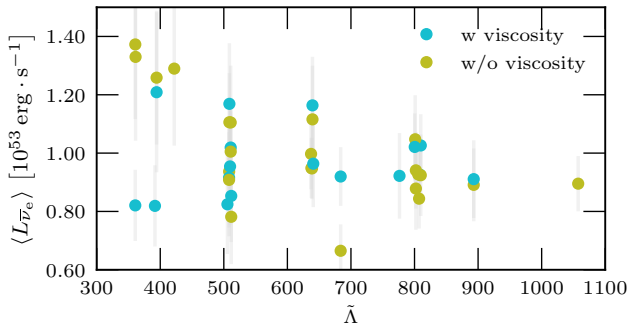

Fig. 12 Same as the middle panel of Fig. 5, but distinguishing simulations which take into account the fluid viscosity by means of the GRLES method from those that do not.

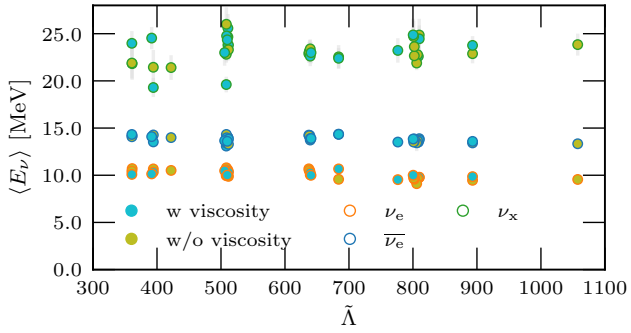

Fig. 13 Same as Fig. 8 with all three panels condensed into one, but distinguishing simulations which take into account the fluid viscosity by means of the GRLES method from those that do not.

Rather interestingly, the figures highlight how the viscosity has essentially no impact on the neutrino emission, at least during the first 10 ms after merger: the points corresponding to viscous simulations are evenly distributed over all values of $\tilde{\Lambda}$ and q. They do not cluster nor show any other particular behaviour.

The explanation is related to the fact that many properties of neutrino emission are influenced primarily by the bulk dynamics of BNS systems and /or by the thermodynamic conditions of matter at the surface of neutrino decoupling, as noted several times in the main text. While the inclusion of viscous effects can have an impact on the bulk dynamics and then on neutrino emission, this requires rather high values of several tens of meters for the mixing length [130]. But in the GRLES model calibrated on MRI data that we employ, the mixing length achieves a moderate value of up to ~ 25 m, and only in a narrow density band: for both higher and lower densities, it decreases rapidly [132]. Therefore the viscosity cannot significantly influence neutrino emission.

Appendix B: Resolution dependence

As discussed in Sec. 3 the simulations used in this study make use of a box-in-box AMR grid with three possible resolutions, namely: LR, SR and HR. Here we study the effect of different resolutions on the neutrino emission by considering one model for which all the three resolutions are available as representative. In each panel of Fig. 14 we present the luminosities obtained by the different simulations for each of the three neutrino species, alongside their sum (bottom right panel). The shaded area represents the maximum variability between resolutions.

On one hand, within the first ~ 10 ms after merger, the three resolutions can differ up to a factor ~ 2 at corresponding times. This is due to the fact that the neutrino luminosity oscillates very rapidly and widely, as a consequence of the complex remnant's dynamics. Clearly point-wise differences become comparable to the oscillation amplitude as soon as the remnant's dynamics (characterized by bounces and sound/shock waves, and strongly dependent on the resolution) accumulates a difference comparable to the luminosity oscillation periods. Enlarging our view on the whole 0-10 ms interval, we recognize that different resolutions produce a very similar global behaviour, even if the HR simulation tends to have higher maximum peaks and lower secondary peaks with respect to the LR one. On the other hand, in the exponentially decreasing phase (after the $10 - 15$ ms mark), the three resolutions show a much closer behaviour.

Finally resolution mainly affects the luminosity peak, while the average luminosities and mean energies are less influenced. In order to quantify their variations, we average the values of $L_{\rm peak}$, $\langle L \rangle$ and $\langle E \rangle$ over the three available resolutions and consider the maximum relative deviations from these values. While peak luminosities can vary by up to 20% from their average value, for average luminosities and average mean energies this figure is reduced to 15% and 8%, respectively.

This analysis suggests that while the precise values we quote in our results could of course be improved if we had access to higher-resolution simulations, the trends we identify are robust and valid.

Appendix C: Data tables

In this section we collect detailed data pertaining to our simulation sample and our results. Table 2 lists PC and VSL simulations, providing details on the initial conditions, EOS and the value of peak luminosities. The same data is provided for DC and LL simulations in

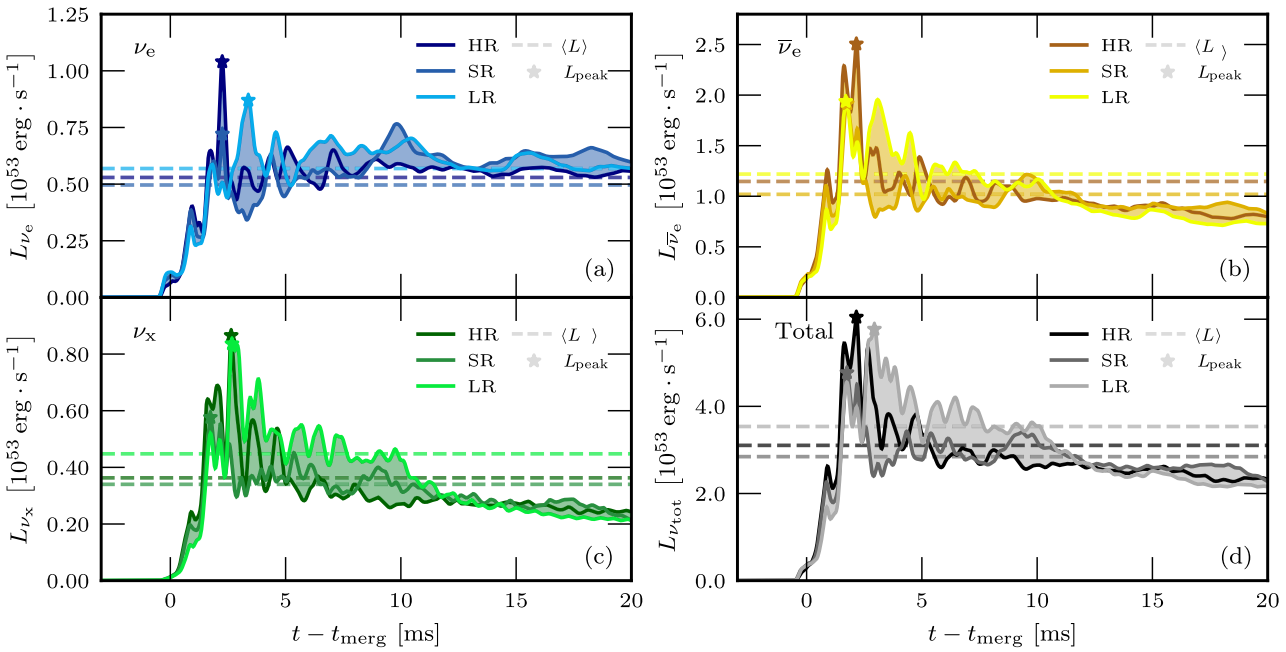

Fig. 14 Resolution comparison for the neutrino luminosity evolution of the three neutrino flavours (ν_e, $\bar{\nu}_e$ and ν_x in panels (a), (b) and (c), respectively) and for the total neutrino luminosity (panel (d)). The model is a LL simulation of an equal mass system ($M_A = M_B = 1.364\,M_\odot$) employing the BLh EOS and GRLES viscosity. Filled regions cover the range containing all three resolutions.

Table 3. In Table 4, we list the values of average luminosities and average mean energies, and their standard deviations for DC and LL simulations.

References

1. A. Perego, S. Bernuzzi, D. Radice, Eur. Phys. J. **A55**(8), 124 (2019). DOI 10.1140/epja/i2019-12810-7
2. M. Shibata, K. Hotokezaka, Ann. Rev. Nucl. Part. Sci. **69**, 41 (2019). DOI 10.1146/annurev-nucl-101918-023625
3. D. Radice, S. Bernuzzi, A. Perego, Ann. Rev. Nucl. Part. Sci. **70** (2020). DOI 10.1146/annurev-nucl-013120-114541
4. L. Baiotti, L. Rezzolla, Rept. Prog. Phys. **80**(9), 096901 (2017). DOI 10.1088/1361-6633/aa67bb
5. B.P. Abbott, et al., Phys. Rev. **X9**(3), 031040 (2019). DOI 10.1103/PhysRevX.9.031040
6. R. Abbott, et al., Astrophys. J. Lett. **915**(1), L5 (2021). DOI 10.3847/2041-8213/ac082e
7. J. Aasi, et al., Class. Quant. Grav. **32**, 074001 (2015). DOI 10.1088/0264-9381/32/7/074001
8. F. Acernese, et al., Class. Quant. Grav. **32**(2), 024001 (2015). DOI 10.1088/0264-9381/32/2/024001
9. Y. Aso, Y. Michimura, K. Somiya, M. Ando, O. Miyakawa, T. Sekiguchi, D. Tatsumi, H. Yamamoto, Phys. Rev. D **88**(4), 043007 (2013). DOI 10.1103/PhysRevD.88.043007
10. D. Eichler, M. Livio, T. Piran, D.N. Schramm, Nature **340**, 126 (1989). DOI 10.1038/340126a0
11. R. Narayan, B. Paczynski, T. Piran, Astrophys. J. **395**, L83 (1992)
12. W.H. Lee, E. Ramirez-Ruiz, New J. Phys. **9**, 17 (2007). DOI 10.1088/1367-2630/9/1/017
13. E. Nakar, Phys. Rept. **442**, 166 (2007). DOI 10.1016/j.physrep.2007.02.005
14. L.X. Li, B. Paczynski, Astrophys.J. **507**, L59 (1998). DOI 10.1086/311680
15. S.R. Kulkarni, (2005)
16. R. Fernández, B.D. Metzger, Ann. Rev. Nucl. Part. Sci. **66**, 23 (2016). DOI 10.1146/annurev-nucl-102115-044819
17. B.D. Metzger, Living Rev. Rel. **23**(1), 1 (2020). DOI 10.1007/s41114-019-0024-0
18. J.J. Cowan, C. Sneden, J.E. Lawler, A. Aprahamian, M. Wiescher, K. Langanke, G. Martínez-Pinedo, F.K. Thielemann, (2019)
19. A. Perego, F.K. Thielemann, G. Cescutti, (2021). DOI 10.1007/978-981-15-4702-7_13-1
20. O. Korobkin, S. Rosswog, A. Arcones, C. Winteler, Mon. Not. Roy. Astron. Soc. **426**, 1940

EOS	M_A $[M_\odot]$	M_B $[M_\odot]$	q	$\tilde{\Lambda}$	Visc	Res	$t_{\rm BH}$ ($t_{\rm end}$) [ms]	$L_{\rm Peak}$ $[10^{53}\,{\rm erg}\cdot{\rm s}^{-1}]$ $\nu_{\rm e}$	$\bar{\nu}_{\rm e}$	$\nu_{\rm x}$	Reference
Prompt collapse											
BLh	1.856	1.020	1.820	504	✓	SR	1.034 (9.489)	0.267	0.579	0.215	[101]
BLh	1.856	1.020	1.820	504	✗	SR	1.128 (2.394)	0.237	0.515	0.205	[101]
BLh	1.914	1.437	1.332	135	✗	SR	0.377 (17.495)	0.134	0.266	0.050	[136]
BLh	1.795	1.527	1.176	131	✗	SR	0.400 (21.321)	0.150	0.219	0.041	[136]
BLh	1.750	1.557	1.124	133	✗	SR	17.518 (25.888)	0.248	0.202	0.034	[136]
BLh	1.654	1.654	1.000	130	✗	SR	0.399 (12.294)	0.107	0.212	0.032	[136]
DD2	1.654	1.654	1.000	258	✗	SR	2.907 (2.883)	0.157	0.529	0.165	[136]
DD2	1.795	1.527	1.176	257	✗	SR	1.589 (8.3)	0.146	0.538	0.156	[136]
DD2	1.914	1.437	1.332	254	✗	SR	1.06 (2.895)	0.138	0.456	0.120	[136]
DD2	2.149	1.289	1.667	248	✗	SR	0.580 (1.259)	0.160	0.437	0.084	[136]
LS220	1.772	1.065	1.664	638	✗	SR	1.515 (9.503)	0.323	0.863	0.444	[101]
LS220	1.772	1.065	1.664	638	✓	LR	1.374 (14.293)	0.323	0.539	0.168	[101]
SFHo	1.772	1.065	1.664	386	✓	SR	1.609 (1.609)	0.527	0.493	0.066	[101]
SFHo	1.795	1.527	1.176	103	✗	LR	0.306 (5.067)	0.244	0.233	0.051	[136]
SFHo	1.795	1.527	1.176	103	✗	SR	0.412 (12.303)	0.180	0.213	0.040	[136]
SFHo	1.654	1.654	1.000	102	✗	SR	0.317 (10.247)	0.161	0.192	0.037	[136]
SFHo	1.914	1.437	1.332	105	✗	SR	0.307 (16.365)	0.196	0.276	0.052	[136]
SLy4	1.772	1.065	1.664	358	✓	SR	0.797 (5.732)	0.178	0.476	0.107	[101]
SLy4	1.856	1.020	1.820	357	✓	LR	0.637 (5.969)	0.202	0.551	0.163	[101]
SLy4	1.654	1.654	1.000	89	✗	SR	0.282 (7.475)	0.182	0.170	0.037	[136]
SLy4	1.795	1.527	1.176	91	✗	SR	0.27 (8.476)	0.186	0.181	0.040	[136]
SLy4	1.914	1.437	1.332	93	✗	SR	0.259 (7.735)	0.180	0.207	0.050	[136]
Very short lived											
SFHo	1.364	1.364	1.000	395	✗	SR	3.313 (7.634)	1.638	4.984	1.589	[101]
SFHo	1.364	1.364	1.000	395	✓	SR	4.69 (22.715)	1.138	3.781	1.118	[101]
SLy4	1.364	1.364	1.000	361	✓	SR	2.136 (10.128)	0.600	2.650	1.215	[101]
SLy4	1.364	1.364	1.000	361	✓	SR	2.147 (7.14)	1.181	3.975	1.604	[101]

Table 2 List of PC and VSL simulations. Columns from left to right provide: the mass of the heaviest star; the mass of the lightest star; the mass ratio; the reduced dimensionless tidal deformability; whether the simulation employs GRLES viscosity; the resolution; the time of collapse (and the time of the end of the simulation); the peal luminosity for the 3 neutrino flavors; the work in which the simulation was first presented.

(2012). DOI 10.1111/j.1365-2966.2012.21859.x

21. S. Rosswog, J. Sollerman, U. Feindt, A. Goobar, O. Korobkin, R. Wollaeger, C. Fremling, M.M. Kasliwal, Astron. Astrophys. **615**, A132 (2018). DOI 10.1051/0004-6361/201732117
22. D. Kasen, B. Metzger, J. Barnes, E. Quataert, E. Ramirez-Ruiz, Nature (2017). DOI 10.1038/nature24453. [Nature551,80(2017)]
23. M.R. Drout, et al., Science **6370**, 1570 (2017). DOI 10.1126/science.aaq0049
24. B.P. Abbott, et al., Phys. Rev. Lett. **119**(16), 161101 (2017). DOI 10.1103/PhysRevLett.119.161101
25. B. Abbott, et al., Astrophys. J. Lett. **848**(2), L12 (2017). DOI 10.3847/2041-8213/aa91c9
26. I. Arcavi, C. McCully, G. Hosseinzadeh, D.A. Howell, S. Vasylyev, D. Poznanski, M. Zaltzman, D. Maoz, L. Singer, S. Valenti, D. Kasen, J. Barnes, T. Piran, W.f. Fong, Astrophysical Journal Letters **848**(2), L33 (2017). DOI 10.3847/2041-8213/aa910f
27. R. Chornock, et al., Astrophys. J. **848**(2), L19 (2017). DOI 10.3847/2041-8213/aa905c
28. P.S. Cowperthwaite, et al., Astrophys. J. **848**(2), L17 (2017). DOI 10.3847/2041-8213/aa8fc7
29. D.A. Coulter, et al., Science (2017). DOI 10.1126/science.aap9811. [Science358,1556(2017)]
30. P.A. Evans, et al., (2017). DOI 10.1126/science.aap9580
31. A. Goldstein, et al., Astrophys. J. **848**(2), L14 (2017). DOI 10.3847/2041-8213/aa8f41
32. G. Hallinan, et al., (2017). DOI 10.1126/science.aap9855
33. M.M. Kasliwal, et al., (2017). DOI 10.1126/science.aap9455
34. A. Murguia-Berthier, et al., (2017). DOI 10.3847/2041-8213/aa91b3
35. M. Nicholl, et al., Astrophys. J. **848**, L18 (2017). DOI 10.3847/2041-8213/aa9029

EOS	M_A $[M_\odot]$	M_B $[M_\odot]$	q	$\tilde{\Lambda}$	Visc	Res	$t_{\rm BH}$ ($t_{\rm end}$) [ms]	$L_{\rm Peak}$ $[10^{53}\,{\rm erg\cdot s^{-1}}]$ $\nu_{\rm e}$	$\bar{\nu}_{\rm e}$	$\nu_{\rm x}$	Reference
Delayed collapse											
LS220	1.350	1.350	1.000	684	✗	SR	22.714 (27.824)	0.500	1.274	0.417	[1]
LS220	1.350	1.350	1.000	684	✓	SR	18.264 (35.064)	0.642	1.487	0.505	[1]
LS220	1.364	1.364	1.000	639	✗	SR	15.475 (32.669)	0.668	1.623	0.457	[134]
LS220	1.400	1.330	1.053	637	✗	SR	16.687 (23.163)	0.732	1.711	0.613	[135]
LS220	1.435	1.298	1.106	638	✗	SR	16.393 (24.964)	0.591	1.522	0.492	[135]
LS220	1.469	1.268	1.159	639	✓	SR	19.89 (33.146)	0.706	2.404	0.872	[135]
LS220	1.635	1.146	1.427	641	✓	SR	11.768 (11.768)	0.770	2.288	0.773	[135]
SFHo	1.350	1.350	1.000	422	✗	SR	7.492 (28.142)	1.649	5.409	1.736	This work
SFHo	1.452	1.283	1.132	394	✗	SR	10.836 (11.821)	0.832	2.946	0.929	[135]
SFHo	1.452	1.283	1.132	394	✓	SR	5.703 (5.703)	0.679	3.037	0.948	[135]
SLy4	1.364	1.364	1.000	361	✗	SR	13.367 (21.903)	1.431	3.996	1.580	[135]
SLy4	1.452	1.283	1.132	361	✗	SR	12.461 (12.461)	0.976	3.362	1.090	[135]
Long lived											
BHB$\Lambda\phi$	1.364	1.364	1.000	808	✓	LR	>27.868	0.504	1.212	0.268	This work
BLh	1.364	1.364	1.000	511	✓	SR	>91.365	0.769	1.923	0.578	[101]
BLh	1.364	1.364	1.000	511	✗	LR	>36.737	1.045	2.669	0.697	[135]
BLh	1.364	1.364	1.000	511	✗	HR	>51.634	0.930	2.098	0.511	This work
BLh	1.364	1.364	1.000	511	✗	SR	>97.211	1.075	3.107	0.850	[135]
BLh	1.482	1.259	1.177	509	✓	LR	>69.074	0.678	2.142	0.804	[135]
BLh	1.482	1.259	1.177	509	✗	LR	>28.167	0.714	1.999	0.809	[135]
BLh	1.581	1.184	1.335	508	✓	SR	>9.683	0.626	2.130	0.576	[135]
BLh	1.581	1.184	1.335	508	✗	LR	>17.493	0.559	1.843	0.532	[135]
BLh	1.699	1.104	1.539	512	✓	LR	>45.546	0.685	1.965	0.646	[135]
BLh	1.699	1.104	1.539	512	✗	LR	>29.613	0.666	1.942	0.573	[135]
BLh	1.772	1.065	1.664	506	✓	SR	>19.987	0.914	2.118	0.844	[101]
BLh	1.635	1.146	1.427	510	✓	SR	>59.32	1.031	2.598	0.690	[135]
DD2	1.300	1.300	1.000	1057	✗	LR	>70.012	0.515	1.248	0.284	This work
DD2	1.364	1.364	1.000	810	✗	SR	>96.698	0.670	1.677	0.446	[134]
DD2	1.364	1.364	1.000	810	✓	SR	>112.545	0.678	1.442	0.355	[134]
DD2	1.432	1.300	1.102	807	✗	LR	>41.494	0.511	1.451	0.351	This work
DD2	1.435	1.298	1.106	806	✗	LR	>13.504	0.478	1.553	0.316	This work
DD2	1.486	1.254	1.185	802	✗	LR	>28.276	0.533	1.691	0.297	This work
DD2	1.486	1.254	1.185	802	✗	HR	>58.463	0.614	1.736	0.281	This work
DD2	1.497	1.245	1.202	801	✗	SR	>88.586	0.586	2.142	0.356	[135]
DD2	1.509	1.235	1.222	800	✓	SR	>85.657	0.592	1.654	0.332	[135]
DD2	1.635	1.146	1.427	776	✓	LR	>37.477	0.551	1.711	0.411	[135]
LS220	1.400	1.200	1.167	893	✗	SR	>24.677	0.549	1.735	0.413	[88]
LS220	1.400	1.200	1.167	893	✓	SR	>48.494	0.573	1.707	0.395	[1]
LS220	1.469	1.268	1.159	639	✗	SR	>35.937	0.734	2.310	0.683	[135]
SFHo	1.635	1.146	1.427	392	✓	SR	>42.141	0.604	2.074	0.510	[135]
SLy4	1.635	1.146	1.427	361	✓	SR	>40.118	0.504	1.587	0.548	[135]

Table 3 List of DC and LL simulations. Columns from left to right provide: the mass of the heaviest star; the mass of the lightest star; the mass ratio; the reduced dimensionless tidal deformability; whether the simulation employs GRLES viscosity; the resolution; the time of collapse (and the time of the end of the simulation); the peal luminosity for the 3 neutrino flavors; the work in which the simulation was first presented.

36. S.J. Smartt, et al., Nature (2017). DOI 10.1038/nature24303
37. M. Soares-Santos, et al., Astrophys. J. **848**(2), L16 (2017). DOI 10.3847/2041-8213/aa9059
38. V. Savchenko, et al., Astrophys. J. **848**(2), L15 (2017). DOI 10.3847/2041-8213/aa8f94
39. N.R. Tanvir, et al., Astrophys. J. **848**, L27 (2017). DOI 10.3847/2041-8213/aa90b6
40. M. Tanaka, et al., Publ. Astron. Soc. Jap. (2017). DOI 10.1093/pasj/psx121
41. E. Troja, et al., Nature (2017). DOI 10.1038/nature24290
42. V.A. Villar, et al., Astrophys. J. **851**(1), L21 (2017). DOI 10.3847/2041-8213/aa9c84
43. E. Waxman, E.O. Ofek, D. Kushnir, A. Gal-Yam, Mon. Not. Roy. Astron. Soc. **481**(3), 3423 (2018). DOI 10.1093/mnras/sty2441

EOS	M_A	M_B	$\tilde{\Lambda}$	Visc	Res	$\langle L \rangle$ $[10^{53}\,\mathrm{erg\cdot s^{-1}}]$			$\sigma_{\langle L \rangle}$ $[10^{53}\,\mathrm{erg\cdot s^{-1}}]$			$\langle E \rangle$ [MeV]			$\sigma_{\langle E \rangle}$ [MeV]		
	$[M_\odot]$	$[M_\odot]$				ν_e	$\bar{\nu}_\mathrm{e}$	ν_x	ν_e	$\bar{\nu}_\mathrm{e}$	ν_x	ν_e	$\bar{\nu}_\mathrm{e}$	ν_x	ν_e	$\bar{\nu}_\mathrm{e}$	ν_x
Delayed collapse																	
LS220	1.350	1.350	684	✗	SR	0.267	0.665	0.231	0.033	0.090	0.033	9.571	14.344	22.546	0.256	0.373	1.248
LS220	1.350	1.350	684	✓	SR	0.460	0.920	0.272	0.045	0.101	0.034	10.672	14.341	22.393	0.431	0.573	1.075
LS220	1.364	1.364	639	✗	SR	0.450	0.948	0.280	0.048	0.105	0.033	10.489	14.222	23.220	0.171	0.288	1.115
LS220	1.400	1.330	637	✗	SR	0.486	0.997	0.312	0.057	0.121	0.049	10.678	14.250	22.880	0.313	0.502	0.936
LS220	1.435	1.298	638	✗	SR	0.422	0.949	0.296	0.044	0.103	0.035	10.507	14.189	23.043	0.141	0.194	1.106
LS220	1.469	1.268	639	✓	SR	0.465	1.164	0.390	0.048	0.166	0.074	10.263	13.877	22.621	0.267	0.264	1.062
LS220	1.635	1.146	641	✓	SR	0.393	0.964	0.372	0.051	0.149	0.059	9.997	13.900	22.990	0.095	0.180	1.135
SFHo	1.350	1.350	422	✗	SR	0.481	1.401	0.533	0.136	0.426	0.142	10.010	13.688	19.916	0.346	0.427	0.656
SFHo	1.350	1.350	422	✗	SR	0.517	1.290	0.486	0.104	0.264	0.098	10.511	13.990	21.411	0.282	0.287	1.306
SFHo	1.452	1.283	394	✗	SR	0.510	1.259	0.506	0.098	0.229	0.099	10.668	14.265	21.443	0.564	0.602	1.835
SFHo	1.452	1.283	394	✓	SR	0.383	1.209	0.430	0.082	0.274	0.113	10.338	13.533	19.296	0.677	0.512	1.010
SLy4	1.364	1.364	361	✗	SR	0.552	1.330	0.570	0.123	0.287	0.124	10.704	14.178	21.824	0.516	0.486	1.707
SLy4	1.452	1.283	361	✗	SR	0.532	1.373	0.527	0.095	0.256	0.097	10.426	14.078	21.889	0.372	0.324	1.631
Long lived																	
BHB$\Lambda\phi$	1.364	1.364	808	✓	LR	0.378	0.926	0.190	0.043	0.094	0.027	9.770	13.509	22.602	0.205	0.291	0.711
BLh	1.364	1.364	511	✓	SR	0.495	1.019	0.340	0.075	0.135	0.051	10.386	13.991	25.587	0.168	0.181	1.501
BLh	1.364	1.364	511	✗	LR	0.523	1.105	0.381	0.095	0.195	0.074	10.449	13.717	23.804	0.146	0.201	0.689
BLh	1.364	1.364	511	✗	HR	0.473	1.005	0.309	0.076	0.137	0.049	10.550	14.014	24.661	0.120	0.186	0.748
BLh	1.365	1.365	508	✗	SR	0.653	0.937	0.345	0.017	0.042	0.030	10.789	14.324	26.001	0.132	0.380	1.798
BLh	1.482	1.259	509	✓	LR	0.471	1.169	0.408	0.063	0.208	0.086	10.577	13.969	24.769	0.189	0.291	1.222
BLh	1.482	1.259	509	✗	LR	0.462	1.106	0.399	0.081	0.168	0.076	10.155	13.631	23.094	0.146	0.225	1.000
BLh	1.581	1.184	508	✓	SR	0.358	0.916	0.303	0.056	0.201	0.069	9.956	13.092	19.612	0.185	0.251	0.827
BLh	1.581	1.184	508	✗	LR	0.344	0.908	0.323	0.045	0.163	0.061	10.006	13.412	22.818	0.135	0.223	0.887
BLh	1.699	1.104	512	✓	LR	0.404	0.853	0.331	0.053	0.158	0.063	10.324	13.839	23.804	0.142	0.157	0.538
BLh	1.699	1.104	512	✗	LR	0.348	0.782	0.280	0.051	0.162	0.059	9.881	13.284	23.301	0.217	0.217	1.128
BLh	1.772	1.065	506	✓	SR	0.382	0.825	0.359	0.066	0.170	0.079	10.474	13.664	22.993	0.368	0.456	1.384
BLh	1.635	1.146	510	✓	SR	0.380	0.954	0.328	0.074	0.200	0.075	10.011	13.597	24.352	0.236	0.224	1.166
DD2	1.300	1.300	1057	✗	LR	0.362	0.895	0.174	0.045	0.095	0.022	9.554	13.336	23.844	0.284	0.386	1.166
DD2	1.364	1.364	810	✗	SR	0.355	0.924	0.195	0.054	0.140	0.038	9.773	13.876	24.859	0.248	0.428	1.719
DD2	1.364	1.364	810	✓	SR	0.419	1.026	0.216	0.055	0.107	0.031	9.790	13.750	24.456	0.216	0.399	1.421
DD2	1.432	1.300	807	✗	LR	0.359	0.844	0.170	0.039	0.102	0.030	9.664	13.658	22.782	0.333	0.506	1.311
DD2	1.435	1.298	806	✗	LR	0.354	0.927	0.181	0.037	0.105	0.025	9.107	13.434	21.889	0.477	0.874	0.749
DD2	1.486	1.254	802	✗	LR	0.336	0.878	0.174	0.038	0.141	0.030	9.585	13.605	22.659	0.228	0.335	1.308
DD2	1.486	1.254	802	✗	HR	0.341	0.941	0.161	0.051	0.131	0.025	9.769	13.846	23.628	0.185	0.348	1.177
DD2	1.497	1.245	801	✗	SR	0.356	1.047	0.206	0.045	0.151	0.031	9.709	13.517	24.696	0.278	0.355	1.676
DD2	1.509	1.235	800	✓	SR	0.361	1.021	0.223	0.043	0.115	0.028	10.002	13.842	24.871	0.372	0.513	1.708
DD2	1.635	1.146	776	✓	LR	0.311	0.922	0.185	0.040	0.147	0.036	9.535	13.518	23.226	0.262	0.358	1.294
LS220	1.400	1.200	893	✗	SR	0.341	0.891	0.214	0.037	0.125	0.032	9.463	13.426	22.881	0.147	0.354	1.022
LS220	1.400	1.200	893	✓	SR	0.356	0.911	0.207	0.035	0.133	0.033	9.852	13.589	23.761	0.217	0.254	0.985
LS220	1.469	1.268	639	✗	SR	0.423	1.116	0.315	0.054	0.184	0.059	10.046	13.729	23.392	0.322	0.266	0.999
SFHo	1.635	1.146	392	✓	SR	0.304	0.819	0.247	0.039	0.139	0.046	10.141	14.091	24.535	0.174	0.295	1.176
SLy4	1.635	1.146	361	✓	SR	0.323	0.821	0.268	0.035	0.122	0.048	10.088	14.323	23.983	0.141	0.190	1.299

Table 4 List of DC and LL simulations. Columns from left to right provide: the mass of the heaviest star; the mass of the lightest star; the reduced dimensionless tidal deformability; whether the simulation employs GRLES viscosity; the resolution; the average luminosity for the 3 neutrino flavors and respective standard deviations; the average mean energy for the 3 neutrino flavors and respective standard deviations.

44. M.M. Kasliwal, et al., (2018). DOI 10.1093/mnrasl/slz007
45. E. Waxman, E.O. Ofek, D. Kushnir, (2019)
46. B. Abbott, et al., Astrophys. J. Lett. **892**, L3 (2020). DOI 10.3847/2041-8213/ab75f5
47. M. Ruffert, H. Janka, K. Takahashi, G. Schäfer, Astron.Astrophys. **319**, 122 (1997)
48. S. Rosswog, E. Ramirez-Ruiz, Mon.Not.Roy.Astron.Soc. **336**, L7 (2002). DOI 10.1046/j.1365-8711.2002.05898.x
49. I. Zalamea, A.M. Beloborodov, Mon. Not. Roy. Astron. Soc. **410**, 2302 (2011). DOI 10.1111/j.1365-2966.2010.17600.x
50. L. Dessart, C. Ott, A. Burrows, S. Rosswog, E. Livne, Astrophys.J. **690**, 1681 (2009). DOI 10.1088/0004-637X/690/2/1681
51. O. Just, M. Obergaulinger, H.T. Janka, A. Bauswein, N. Schwarz, Astrophys. J. Lett. **816**(2), L30 (2016). DOI 10.3847/2041-8205/816/2/L30
52. A. Perego, H. Yasin, A. Arcones, J. Phys. **G44**(8), 084007 (2017). DOI 10.1088/1361-6471/aa7bdc
53. S. Fujibayashi, Y. Sekiguchi, K. Kiuchi, M. Shibata, Astrophys. J. **846**(2), 114 (2017). DOI 10.3847/1538-4357/aa8039
54. A. Perego, A. Arcones, D. Martin, H. Yasin, JPS Conf. Proc. **14**, 020810 (2017). DOI 10.7566/JPSCP.14.020810
55. B.D. Metzger, R. Fernández, Mon.Not.Roy.Astron.Soc. **441**, 3444 (2014).

DOI 10.1093/mnras/stu802
56. D. Martin, A. Perego, A. Arcones, F.K. Thielemann, O. Korobkin, S. Rosswog, Astrophys. J. **813**(1), 2 (2015). DOI 10.1088/0004-637X/813/1/2
57. J.M. Miller, B.R. Ryan, J.C. Dolence, A. Burrows, C.J. Fontes, C.L. Fryer, O. Korobkin, J. Lippuner, M.R. Mumpower, R.T. Wollaeger, Phys. Rev. **D100**(2), 023008 (2019). DOI 10.1103/PhysRevD.100.023008
58. F. Foucart, E. O'Connor, L. Roberts, L.E. Kidder, H.P. Pfeiffer, M.A. Scheel, Phys. Rev. **D94**(12), 123016 (2016). DOI 10.1103/PhysRevD.94.123016
59. A. Perego, D. Radice, S. Bernuzzi, Astrophys. J. **850**(2), L37 (2017). DOI 10.3847/2041-8213/aa9ab9
60. V. Nedora, F. Schianchi, S. Bernuzzi, D. Radice, B. Daszuta, A. Endrizzi, A. Perego, A. Prakash, F. Zappa, preprint (arXiv:2011.11110) (2020)
61. A. Endrizzi, A. Perego, F.M. Fabbri, L. Branca, D. Radice, S. Bernuzzi, B. Giacomazzo, F. Pederiva, A. Lovato, Eur. Phys. J. A **56**(1), 15 (2020). DOI 10.1140/epja/s10050-019-00018-6
62. S. Rosswog, M. Liebendoerfer, Mon.Not.Roy.Astron.Soc. **342**, 673 (2003). DOI 10.1046/j.1365-8711.2003.06579.x
63. M. Shibata, K. Kiuchi, Y.i. Sekiguchi, Y. Suwa, Prog.Theor.Phys. **125**, 1255 (2011). DOI 10.1143/PTP.125.1255
64. F. Galeazzi, W. Kastaun, L. Rezzolla, J.A. Font, Phys.Rev. **D88**, 064009 (2013). DOI 10.1103/PhysRevD.88.064009
65. A. Perego, R. Cabezon, R. Kaeppeli, Astrophys. J. Suppl. **223**(2), 22 (2016). DOI 10.3847/0067-0049/223/2/22
66. F. Foucart, Mon. Not. Roy. Astron. Soc. **475**(3), 4186 (2018). DOI 10.1093/mnras/sty108
67. R. Ardevol-Pulpillo, H.T. Janka, O. Just, A. Bauswein, Mon. Not. Roy. Astron. Soc. **485**(4), 4754 (2019). DOI 10.1093/mnras/stz613
68. F. Foucart, M.D. Duez, L.E. Kidder, R. Nguyen, H.P. Pfeiffer, M.A. Scheel, Phys. Rev. **D98**(6), 063007 (2018). DOI 10.1103/PhysRevD.98.063007
69. D. Gizzi, E. O'Connor, S. Rosswog, A. Perego, R. Cabezón, L. Nativi, Mon. Not. Roy. Astron. Soc. **490**(3), 4211 (2019). DOI 10.1093/mnras/stz2911
70. L.R. Weih, A. Gabbana, D. Simeoni, L. Rezzolla, S. Succi, R. Tripiccione, "Mon. Not. Roy. Astron. Soc." **498**(3), 3374 (2020). DOI 10.1093/mnras/staa2575
71. F. Foucart, M.D. Duez, F. Hebert, L.E. Kidder, H.P. Pfeiffer, M.A. Scheel, Astrophys. J. Lett. **902**, L27 (2020). DOI 10.3847/2041-8213/abbb87
72. D. Gizzi, C. Lundman, E. O'Connor, S. Rosswog, A. Perego, Mon. Not. Roy. Astron. Soc. **505**(2), 2575 (2021). DOI 10.1093/mnras/stab1432
73. H.T. Janka, (2017). DOI 10.1007/978-3-319-21846-5_4
74. A. Mezzacappa, E. Endeve, O.E.B. Messer, S.W. Bruenn, Living Reviews in Computational Astrophysics **6**(1), 4 (2020). DOI 10.1007/s41115-020-00010-8
75. Y. Sekiguchi, K. Kiuchi, K. Kyutoku, M. Shibata, Phys.Rev. **D91**(6), 064059 (2015). DOI 10.1103/PhysRevD.91.064059
76. C. Palenzuela, S.L. Liebling, D. Neilsen, L. Lehner, O.L. Caballero, E. O'Connor, M. Anderson, Phys. Rev. **D92**(4), 044045 (2015). DOI 10.1103/PhysRevD.92.044045
77. F. Foucart, R. Haas, M.D. Duez, E. O'Connor, C.D. Ott, L. Roberts, L.E. Kidder, J. Lippuner, H.P. Pfeiffer, M.A. Scheel, Phys. Rev. **D93**(4), 044019 (2016). DOI 10.1103/PhysRevD.93.044019
78. M.R. Wu, I. Tamborra, O. Just, H.T. Janka, Phys. Rev. D **96**(12), 123015 (2017). DOI 10.1103/PhysRevD.96.123015
79. M. George, M.R. Wu, I. Tamborra, R. Ardevol-Pulpillo, H.T. Janka, Phys. Rev. D **102**(10), 103015 (2020). DOI 10.1103/PhysRevD.102.103015
80. I. Kullmann, S. Goriely, O. Just, R. Ardevol-Pulpillo, A. Bauswein, H.T. Janka, (2021). DOI 10.1093/mnras/stab3393
81. K. Yagi, N. Yunes, Phys. Rept. **681**, 1 (2017). DOI 10.1016/j.physrep.2017.03.002
82. Z. Carson, K. Chatziioannou, C.J. Haster, K. Yagi, N. Yunes, Phys. Rev. **D99**(8), 083016 (2019). DOI 10.1103/PhysRevD.99.083016
83. V. Paschalidis, K. Yagi, D. Alvarez-Castillo, D.B. Blaschke, A. Sedrakian, Phys. Rev. **D97**(8), 084038 (2018). DOI 10.1103/PhysRevD.97.084038
84. P. Pani, L. Gualtieri, V. Ferrari, (2015)
85. L. Rezzolla, K. Takami, Phys. Rev. **D93**(12), 124051 (2016). DOI 10.1103/PhysRevD.93.124051
86. D.A. Godzieba, R. Gamba, D. Radice, S. Bernuzzi, (2020)
87. S. Bernuzzi, A. Nagar, S. Balmelli, T. Dietrich, M. Ujevic, Phys.Rev.Lett. **112**, 201101 (2014). DOI 10.1103/PhysRevLett.112.201101
88. D. Radice, A. Perego, K. Hotokezaka, S.A. Fromm, S. Bernuzzi, L.F. Roberts, Astrophys. J. **869**(2), 130 (2018). DOI 10.3847/1538-4357/aaf054
89. F. Loffler, et al., Class. Quant. Grav. **29**, 115001 (2012). DOI 10.1088/0264-9381/29/11/115001

90. E. Schnetter, S.H. Hawley, I. Hawke, Class.Quant.Grav. **21**, 1465 (2004). DOI 10.1088/0264-9381/21/6/014
91. C. Reisswig, R. Haas, C.D. Ott, E. Abdikamalov, P. Mösta, D. Pollney, E. Schnetter, Phys. Rev. **D87**(6), 064023 (2013). DOI 10.1103/PhysRevD.87.064023
92. S. Bernuzzi, D. Hilditch, Phys. Rev. **D81**, 084003 (2010). DOI 10.1103/PhysRevD.81.084003
93. D. Pollney, C. Reisswig, E. Schnetter, N. Dorband, P. Diener, Phys. Rev. **D83**, 044045 (2011). DOI 10.1103/PhysRevD.83.044045
94. C. Reisswig, C. Ott, E. Abdikamalov, R. Haas, P. Mösta, et al., Phys.Rev.Lett. **111**, 151101 (2013). DOI 10.1103/PhysRevLett.111.151101
95. D. Radice, L. Rezzolla, Astron. Astrophys. **547**, A26 (2012). DOI 10.1051/0004-6361/201219735
96. D. Radice, L. Rezzolla, F. Galeazzi, Mon.Not.Roy.Astron.Soc. **437**, L46 (2014). DOI 10.1093/mnrasl/slt137
97. D. Radice, L. Rezzolla, F. Galeazzi, Class.Quant.Grav. **31**, 075012 (2014). DOI 10.1088/0264-9381/31/7/075012
98. D. Radice, F. Galeazzi, J. Lippuner, L.F. Roberts, C.D. Ott, L. Rezzolla, Mon. Not. Roy. Astron. Soc. **460**(3), 3255 (2016). DOI 10.1093/mnras/stw1227
99. M.J. Berger, J. Oliger, J.Comput.Phys. **53**, 484 (1984)
100. M.J. Berger, P. Colella, Journal of Computational Physics **82**, 64 (1989). DOI 10.1016/0021-9991(89)90035-1
101. S. Bernuzzi, et al., Mon. Not. Roy. Astron. Soc. (2020). DOI 10.1093/mnras/staa1860
102. M. Favata, S.A. Hughes, D.E. Holz, Astrophys. J. **607**, L5 (2004). DOI 10.1086/421552
103. T. Hinderer, "Astrophys. J." **677**(2), 1216 (2008). DOI 10.1086/533487
104. E. Gourgoulhon, P. Grandclement, S. Bonazzola, Phys. Rev. **D65**, 044020 (2002). DOI 10.1103/PhysRevD.65.044020
105. M. Ruffert, M. Rampp, H.T. Janka, arXiv preprint (1996)
106. S. Rosswog, E. Ramirez-Ruiz, M.B. Davies, Mon. Not. Roy. Astron. Soc. **345**, 1077 (2003). DOI 10.1046/j.1365-2966.2003.07032.x
107. T.A. Thompson, A. Burrows, P.A. Pinto, Astrophys. J. **592**, 434 (2003). DOI 10.1086/375701
108. A. Burrows, S. Reddy, T.A. Thompson, Nucl. Phys. **A777**, 356 (2006). DOI 10.1016/j.nuclphysa.2004.06.012
109. D. Neilsen, S.L. Liebling, M. Anderson, L. Lehner, E. O'Connor, et al., Phys.Rev. **D89**(10), 104029 (2014). DOI 10.1103/PhysRevD.89.104029
110. S.W. Bruenn, Astrophys. J. Suppl. **58**, 771 (1985). DOI 10.1086/191056
111. S.L. Shapiro, S.A. Teukolsky, *Black holes, white dwarfs, and neutron stars: The physics of compact objects* (1983)
112. J.M. Lattimer, F.D. Swesty, Nucl. Phys. **A535**, 331 (1991). DOI 10.1016/0375-9474(91)90452-C
113. F. Douchin, P. Haensel, Astron. Astrophys. **380**, 151 (2001)
114. A.S. Schneider, L.F. Roberts, C.D. Ott, Phys. Rev. **C96**(6), 065802 (2017). DOI 10.1103/PhysRevC.96.065802
115. S. Typel, G. Ropke, T. Klahn, D. Blaschke, H.H. Wolter, Phys. Rev. **C81**, 015803 (2010). DOI 10.1103/PhysRevC.81.015803
116. M. Hempel, J. Schaffner-Bielich, Nucl. Phys. **A837**, 210 (2010). DOI 10.1016/j.nuclphysa.2010.02.010
117. A.W. Steiner, J.M. Lattimer, E.F. Brown, Astrophys. J. **765**, L5 (2013). DOI 10.1088/2041-8205/765/1/L5
118. S. Banik, M. Hempel, D. Bandyopadhyay, Astrophys. J. Suppl. **214**(2), 22 (2014). DOI 10.1088/0067-0049/214/2/22
119. D. Logoteta, A. Perego, I. Bombaci, Astron. Astrophys. **646**, A55 (2021). DOI 10.1051/0004-6361/202039457
120. B.P. Abbott, et al., Phys. Rev. Lett. **121**(16), 161101 (2018). DOI 10.1103/PhysRevLett.121.161101
121. B.P. Abbott, R. Abbott, T.D. Abbott, S. Abraham, LIGO Scientific Collaboration, Virgo Collaboration, Physical Review D **100**(10), 104036 (2019). DOI 10.1103/PhysRevD.100.104036
122. S. De, D. Finstad, J.M. Lattimer, D.A. Brown, E. Berger, C.M. Biwer, Phys. Rev. Lett. **121**(9), 091102 (2018). DOI 10.1103/PhysRevLett.121.259902,10.1103/PhysRevLett.121.091102. [Erratum: Phys. Rev. Lett.121,no.25,259902(2018)]
123. M.B. Tsang, et al., Phys. Rev. C **86**, 015803 (2012). DOI 10.1103/PhysRevC.86.015803
124. J.M. Lattimer, Y. Lim, Astrophys. J. **771**, 51 (2013). DOI 10.1088/0004-637X/771/1/51
125. D. Adhikari, et al., Phys. Rev. Lett. **126**(17), 172502 (2021). DOI 10.1103/PhysRevLett.126.172502
126. I. Bombaci, D. Logoteta, Astron. Astrophys. **609**, A128 (2018). DOI 10.1051/0004-6361/201731604
127. R. Machleidt, D.R. Entem, Phys. Rept. **503**, 1 (2011). DOI 10.1016/j.physrep.2011.02.001
128. M. Piarulli, L. Girlanda, R. Schiavilla, A. Kievsky, A. Lovato, L.E. Marcucci, S.C. Pieper, M. Viviani,

R.B. Wiringa, Phys. Rev. **C94**(5), 054007 (2016). DOI 10.1103/PhysRevC.94.054007
129. D. Logoteta, I. Bombaci, A. Kievsky, Phys. Rev. **C94**(6), 064001 (2016). DOI 10.1103/PhysRevC.94.064001
130. D. Radice, Astrophys. J. **838**(1), L2 (2017). DOI 10.3847/2041-8213/aa6483
131. M.D. Duez, A. Knight, F. Foucart, M. Haddadi, J. Jesse, F. Hebert, L.E. Kidder, H.P. Pfeiffer, M.A. Scheel, Phys. Rev. D **102**(10), 104050 (2020). DOI 10.1103/PhysRevD.102.104050
132. D. Radice, Symmetry **12**(8), 1249 (2020). DOI 10.3390/sym12081249
133. K. Kiuchi, K. Kyutoku, Y. Sekiguchi, M. Shibata, Phys. Rev. **D97**(12), 124039 (2018). DOI 10.1103/PhysRevD.97.124039
134. V. Nedora, S. Bernuzzi, D. Radice, A. Perego, A. Endrizzi, N. Ortiz, Astrophys. J. **886**(2), L30 (2019). DOI 10.3847/2041-8213/ab5794
135. V. Nedora, S. Bernuzzi, D. Radice, B. Daszuta, A. Endrizzi, A. Perego, A. Prakash, M. Safarzadeh, F. Schianchi, D. Logoteta, Astrophys. J. **906**(2), 98 (2021). DOI 10.3847/1538-4357/abc9be
136. Camilletti et al., in preparation (2021)
137. K. Chatziioannou, General Relativity and Gravitation **52**(11), 109 (2020). DOI 10.1007/s10714-020-02754-3
138. D. Lai, Mon. Not. Roy. Astron. Soc. **270**, 611 (1994). DOI 10.1093/mnras/270.3.611
139. A. Perego, S. Rosswog, R. Cabezon, O. Korobkin, R. Kaeppeli, et al., Mon.Not.Roy.Astron.Soc. **443**, 3134 (2014). DOI 10.1093/mnras/stu1352
140. D. Radice, A. Perego, S. Bernuzzi, B. Zhang, Mon. Not. Roy. Astron. Soc. **481**(3), 3670 (2018). DOI 10.1093/mnras/sty2531
141. R. Fernández, B.D. Metzger, Mon. Not. Roy. Astron. Soc. **435**, 502 (2013). DOI 10.1093/mnras/stt1312
142. S. Bernuzzi, D. Radice, C.D. Ott, L.F. Roberts, P. Moesta, F. Galeazzi, Phys. Rev. **D94**(2), 024023 (2016). DOI 10.1103/PhysRevD.94.024023
143. F. Zappa, S. Bernuzzi, D. Radice, A. Perego, T. Dietrich, Phys. Rev. Lett. **120**(11), 111101 (2018). DOI 10.1103/PhysRevLett.120.111101
144. Y. Qian, S. Woosley, Astrophys. J. **471**, 331 (1996). DOI 10.1086/177973
145. D. Martin, A. Perego, W. Kastaun, A. Arcones, Class. Quant. Grav. **35**(3), 034001 (2018). DOI 10.1088/1361-6382/aa9f5a
146. M.H. Ruffert, H.T. Janka, G. Schäfer, Astron. Astrophys. **311**, 532 (1996)
147. S. Rosswog, M. Liebendoerfer, F. Thielemann, M. Davies, W. Benz, et al., Astron.Astrophys. **341**, 499 (1999)
148. S. Rosswog, M.B. Davies, Mon. Not. Roy. Astron. Soc. **345**, 1077 (2003). DOI 10.1046/j.1365-2966.2003.07032.x
149. R. Oechslin, H.T. Janka, A. Marek, Astron.Astrophys. (2006)
150. Y. Sekiguchi, K. Kiuchi, K. Kyutoku, M. Shibata, Phys.Rev.Lett. **107**, 051102 (2011). DOI 10.1103/PhysRevLett.107.051102
151. S. Rosswog, T. Piran, E. Nakar, Mon. Not. Roy. Astron. Soc. **430**, 2585 (2013). DOI 10.1093/mnras/sts708
152. A. Bauswein, S. Goriely, H.T. Janka, Astrophys.J. **773**, 78 (2013). DOI 10.1088/0004-637X/773/1/78
153. L. Lehner, S.L. Liebling, C. Palenzuela, O.L. Caballero, E. O'Connor, M. Anderson, D. Neilsen, Class. Quant. Grav. **33**(18), 184002 (2016). DOI 10.1088/0264-9381/33/18/184002
154. Y. Sekiguchi, K. Kiuchi, K. Kyutoku, M. Shibata, K. Taniguchi, Phys. Rev. **D93**(12), 124046 (2016). DOI 10.1103/PhysRevD.93.124046
155. L. Bovard, D. Martin, F. Guercilena, A. Arcones, L. Rezzolla, O. Korobkin, Phys. Rev. **D96**(12), 124005 (2017). DOI 10.1103/PhysRevD.96.124005
156. T. Vincent, F. Foucart, M.D. Duez, R. Haas, L.E. Kidder, H.P. Pfeiffer, M.A. Scheel, Phys. Rev. **D101**(4), 044053 (2020). DOI 10.1103/PhysRevD.101.044053
157. A. Perego, D. Vescovi, A. Fiore, S. Benetti, S. Bernuzzi, M. Branchesi, S. Cristallo, E. Cappellaro, D. Radice, (2020)
158. B. Metzger, A. Piro, E. Quataert, Mon.Not.Roy.Astron.Soc. **390**, 781 (2008). DOI 10.1111/j.1365-2966.2008.13789.x
159. B.D. Metzger, A.L. Piro, E. Quataert, Mon. Not. Roy. Astron. Soc. **396**, 304 (2009). DOI 10.1111/j.1365-2966.2008.14380.x
160. D.M. Siegel, R. Ciolfi, L. Rezzolla, Astrophys. J. **785**, L6 (2014). DOI 10.1088/2041-8205/785/1/L6
161. O. Just, A. Bauswein, R.A. Pulpillo, S. Goriely, H.T. Janka, Mon. Not. Roy. Astron. Soc. **448**(1), 541 (2015). DOI 10.1093/mnras/stv009
162. S. Fujibayashi, K. Kiuchi, N. Nishimura, Y. Sekiguchi, M. Shibata, Astrophys. J. **860**(1), 64 (2018). DOI 10.3847/1538-4357/aabafd
163. D.M. Siegel, B.D. Metzger, Astrophys. J. **858**(1), 52 (2018). DOI 10.3847/1538-4357/aabaec
164. B.D. Metzger, T.A. Thompson, E. Quataert, Astrophys. J. **856**(2), 101 (2018). DOI 10.3847/

1538-4357/aab095
165. R. Fernández, A. Tchekhovskoy, E. Quataert, F. Foucart, D. Kasen, Mon. Not. Roy. Astron. Soc. **482**(3), 3373 (2019). DOI 10.1093/mnras/sty2932
166. S. Fujibayashi, S. Wanajo, K. Kiuchi, K. Kyutoku, Y. Sekiguchi, M. Shibata, "Astrophys. J." **901**(2), 122 (2020). DOI 10.3847/1538-4357/abafc2
167. R. Ciolfi, J.V. Kalinani, Astrophys. J. Lett. **900**(2), L35 (2020). DOI 10.3847/2041-8213/abb240
168. P. Mösta, D. Radice, R. Haas, E. Schnetter, S. Bernuzzi, arXiv:2003.06043 (2020)
169. O. Just, S. Goriely, H.T. Janka, S. Nagataki, A. Bauswein, (2021). DOI 10.1093/mnras/stab2861
170. M. Shibata, S. Fujibayashi, Y. Sekiguchi, Phys. Rev. D **103**(4), 043022 (2021). DOI 10.1103/PhysRevD.103.043022
171. A. Perego, M. Hempel, C. Fröhlich, K. Ebinger, M. Eichler, J. Casanova, M. Liebendoerfer, F.K. Thielemann, Astrophys. J. **806**(2), 275 (2015). DOI 10.1088/0004-637X/806/2/275
172. S. Richers, H. Nagakura, C.D. Ott, J. Dolence, K. Sumiyoshi, S. Yamada, Astrophys. J. **847**(2), 133 (2017). DOI 10.3847/1538-4357/aa8bb2
173. E. O'Connor, et al., J. Phys. **G45**(10), 104001 (2018). DOI 10.1088/1361-6471/aadeae
174. K.C. Pan, C. Mattes, E.P. O'Connor, S.M. Couch, A. Perego, A. Arcones, J. Phys. **G46**(1), 014001 (2019). DOI 10.1088/1361-6471/aaed51
175. R.M. Cabezón, K.C. Pan, M. Liebendörfer, T. Kuroda, K. Ebinger, O. Heinimann, F.K. Thielemann, A. Perego, Astron. Astrophys. **619**, A118 (2018). DOI 10.1051/0004-6361/201833705
176. C.J. Horowitz, Phys. Rev. **D65**, 043001 (2002). DOI 10.1103/PhysRevD.65.043001
177. L.F. Roberts, S. Reddy, Phys. Rev. **C95**(4), 045807 (2017). DOI 10.1103/PhysRevC.95.045807
178. M. Oertel, A. Pascal, M. Mancini, J. Novak, Phys. Rev. C **102**(3), 035802 (2020). DOI 10.1103/PhysRevC.102.035802
179. A. Malkus, J.P. Kneller, G.C. McLaughlin, R. Surman, Phys. Rev. D **86**, 085015 (2012). DOI 10.1103/PhysRevD.86.085015
180. A. Malkus, G.C. McLaughlin, R. Surman, Phys. Rev. D **93**(4), 045021 (2016). DOI 10.1103/PhysRevD.93.045021
181. Y.L. Zhu, A. Perego, G.C. McLaughlin, Phys. Rev. D **94**(10), 105006 (2016). DOI 10.1103/PhysRevD.94.105006
182. M.R. Wu, I. Tamborra, Phys. Rev. D **95**(10), 103007 (2017). DOI 10.1103/PhysRevD.95.103007
183. S.A. Richers, G.C. McLaughlin, J.P. Kneller, A. Vlasenko, Phys. Rev. D **99**(12), 123014 (2019). DOI 10.1103/PhysRevD.99.123014
184. M. Frensel, M.R. Wu, C. Volpe, A. Perego, Phys. Rev. D **95**(2), 023011 (2017). DOI 10.1103/PhysRevD.95.023011
185. K. Abe, et al., arXiv e-prints arXiv:1805.04163 (2018)